

Hadronic Production of High-Mass Muon Pairs and the Measurement  
of the Pion Structure Function\*

K.J. Anderson, R.N. Coleman, K.P. Karhi, C.B. Newman, J.E. Pilcher,  
and E.I. Rosenberg

Enrico Fermi Institute, University of Chicago, Chicago, Illinois 60637 U.S.A.

J. J. Thaler

University of Illinois, Department of Physics, Urbana, Illinois, 61801 U.S.A.

and

G. E. Hogan, K.T. McDonald, G.H. Sanders,<sup>†</sup> and A.J.S. Smith

Joseph Henry Laboratories, Princeton University, Princeton, New Jersey 08540 U.S.A.

ABSTRACT

Differential cross sections are presented for  $\mu$ -pairs produced in collisions of 225 GeV  $\pi^\pm$  and  $p^\pm$  beams with carbon, copper and tungsten targets. For pair masses  $>4$  GeV, the data are compared with the Drell-Yan model of quark-antiquark annihilation. Excellent agreement is found. Finally, the  $\pi^-$ -induced data are analyzed to give the first measurement of the quark structure function of the pion.

(Paper submitted to the XIX International Conference on High Energy Physics, Tokyo, Japan, 1978.)

## I. Description of the Experiment

We report the first results from a recent experiment at Fermilab in which  $\mu$ -pair production by hadrons was measured with a large-acceptance spectrometer. This work significantly extends our earlier measurements,<sup>1</sup> through the use of higher intensity beams as well as improved detector acceptance and rate-handling capability.

The spectrometer is shown in Fig. 1. An unseparated positive or negative beam of 225 GeV hadrons ( $\pi^\pm$ ,  $p^\pm$ ) was focussed to a spot 2 cm x 3 cm at the experimental target. The beam was defined by scintillation counters placed upstream and downstream of the last set of beam-transport dipole magnets as well as by a counter just upstream of the target. Anti-coincidence counters placed around the beam at several points protected against interactions upstream of the target and largely eliminated triggers involving halo muons. A 3 m thick iron absorber was positioned 1.7 m downstream of the target to shield the spectrometer from hadrons. The muons emerging from the iron traversed a triggering scintillation counter hodoscope J, a set of multiwire proportional chambers (MWPC's) and then entered the cylindrical field of the University of Chicago cyclotron magnet which is 4.2 m in diameter and 1.27 m in gap height. The magnet was set to produce a transverse momentum kick of 1.1 GeV/c. Downstream of the magnet the muons traversed a series of spark chambers, a triggering hodoscope array F, and finally an additional 2.5 m of steel followed by hodoscope array P.

Four threshold gas Cerenkov counters were placed in the beam to identify the particle type. For negative running, all counters were set just below  $\bar{p}$  threshold. For positive beams, the two longest counters were set just below K threshold, the other two just below proton threshold. The negative beam was dominantly  $\pi^-$  mesons, with a  $\bar{p}$  component of  $\sim 0.5\%$ . The positive beam was composed of protons and pions in a ratio of  $\sim 5$  to 1. The pion component was enhanced, at the expense of total transmission, by placing a polyethylene absorber in the beam about 300 meters upstream of the target. The positive beam flux was kept at  $\lesssim 10^7$ /pulse to allow good  $\pi$ -p separation. Negative fluxes up to  $2 \times 10^7$ /pulse were obtained.

Carbon, copper, and tungsten targets, each one-absorption-length thick and 10-cm-wide by 6-cm-high, were used in the experiment. To improve vertex resolution and to monitor possible effects of secondary interactions, the carbon target was divided into three segments of equal thickness, interspersed with scintillation counters. The scintillator pulse heights were used to localize the point of interaction. The only thick target effect which could be of any consequence, the production of  $\mu$ -pairs by secondary particles produced in the target, is suppressed by the steep energy dependence of the production cross section. Such an effect would appear as an excess of counts at low Feynman- $x$  ( $x_F = P_L^*/P_{\max}^*$ ) for the events originating in the downstream target segment. A comparison of the  $x_F$  distributions for 10,000  $J/\psi$  events originating in the upstream and downstream target segments reveals no evidence of secondary interactions.

Upstream of the magnet the particle trajectories were measured by eight M/PC planes, approximately 2-m-wide by 1-m-high. Three measurements were made of each of the X and Y coordinates; in addition, single measurements

were made of U and V coordinates rotated  $45^\circ$  with respect to XY. Downstream of the magnet twelve capacitor-readout spark chamber planes, 2-m-high by 4-m-wide, determined the trajectories.

The trigger requirements demanded the following: (1) A valid beam particle defined by the scintillation counters in the beam and the anti-coincidence counters around the beam. (2)  $\geq$ Two particles leaving the target as indicated by the pulse height in a small scintillation counter placed just downstream of the target. (3) An indication from the horizontal and vertical elements of the J hodoscope array of at least one particle on each side of the beam and one above and below the beam. (4) At least one particle above the beam and one particle below the beam in hodoscope plane F. (5) At least two particles emerging from the final 2.5 m steel shield and striking non-adjacent counters of the P hodoscope. These requirements led to a sample of triggers which consisted almost exclusively of muon pairs produced in the target.

The trigger rate was dominated by low-mass pairs ( $\lesssim 1$  GeV). Such pairs were suppressed by a specially built digital logic system which used the pulses from the J and F hodoscopes (and the assumption that the pairs originated in the target) to estimate the pair mass in  $\approx 100$  ns. Figure 2 sketches the principle of operation. First, we required that the muons occupy opposite quadrants of the J hodoscope (UP-LEFT and DOWN-RIGHT, or DOWN-LEFT and UP-RIGHT), so that hits in the F bank could be correlated with those in the J. The pair mass for each combination of hits was calculated by Monte Carlo studies, and the logic was wired so that only combinations with masses above a selectable threshold would trigger the detector. For the highest threshold used in the experiment, the trigger rate was suppressed by a factor

of 20 with no significant loss in efficiency for  $\mu$ -pairs with masses above 2.7 GeV. The system was closely monitored throughout the run and it performed without incident.

The event reconstruction, which is very similar to that of our previous experiment, is described in detail elsewhere.<sup>2</sup> Aside from the usual track-fitting procedures, we required that all tracks point to struck hodoscope counters, and that these counters satisfy the logic requirements. The muon tracks were required to form a vertex in the target, within resolution. The reconstruction efficiency was estimated by visual scanning of the events to be  $0.92 \pm 0.04$ .

Before describing the results in detail, let us summarize the data. For reasons described below, a carbon target was used with positive and negative beams to measure, among other things, the ratio of  $\mu$ -pair cross sections from  $\pi^+$  and  $\pi^-$  beams incident on an isoscalar target. Following this phase of the running, we used the heavier targets Cu and W to obtain as large a sample of  $\pi^-$ -induced pairs as possible within the brief running time allotted to the experiment.

## II. Properties of the $\mu$ -Pair Cross Section

### (a) Mass Spectrum

Figure 3 shows the mass spectrum measured for a  $\pi^-$  beam incident on nuclear targets. For masses well above the  $J/\psi$ , the shape of the continuum is reasonably represented by the form  $d\sigma/dM \propto \exp[-(.99 \pm .03)M]$ . No conclusive evidence is seen for an enhancement at 9.5 GeV, giving an upper limit for  $T$  production relative to the  $J/\psi$  of  $1.4 \times 10^{-3}$  with 95 per cent confidence. The ratio of  $(T+T')$  to continuum is less than 1.1, over a 2 GeV mass range. This is to be compared with the Columbia-Fermilab Stony Brook (CFS) result<sup>3</sup> for 200 GeV protons:  $(T+T')/\text{continuum} \approx 0.75 \pm 0.75$ . In Fig. 4 the region  $M \lesssim 5$  GeV is shown in more detail.

In particular the  $\psi'(3.7)$  is seen above the continuum. Our results for  $\psi'(3.7)$  production are:

Beam	$B\sigma(\psi')/B\sigma(J/\psi)$
$\pi^+$	$.017 \pm .009$
$\pi^-$	$.021 \pm .006$
p	$.016 \pm .009$

Although this paper emphasizes the continuum, we now mention our measurement of the cross section for  $\bar{p}C \rightarrow J/\psi + X$ . On the basis of 46 events we find

$$\frac{\sigma(\bar{p}C \rightarrow J/\psi + X)}{\sigma(pC \rightarrow J/\psi + X)} = 1.2 \pm 0.6, \text{ where}$$

the error is dominated by uncertainty in normalization. No events were observed with masses above the  $J/\psi$ , providing a weak limit on the magnitude of the  $\bar{p}$ -induced continuum.

(b) Dependence on  $x_F$

The relative cross section  $d\sigma/dx_F$  for  $\pi^-$ -induced pairs is shown in Fig. 5a, for several mass intervals extending from the  $J/\psi$  up to  $M > 8.5$  GeV. The striking effect is seen that as the pair mass increases, the  $x_F$  spectrum becomes progressively flatter. We note that the definition of  $x_F$  used in Fig. 5 takes into account the creation of the massive pair. At  $M_{\mu\mu} = 8.5$  GeV, for example,  $p_{\max}^* = 0.83\sqrt{s}/2$ . Although the proton-induced data are much sparser, the  $x_F$ -distributions of Fig. 5b show similar behaviour. At the  $J/\psi$  mass, the fit to  $(1-x_F)^a$  gives  $a = 4.30 \pm 0.10$ , whereas in the mass range  $3.5 < M < 4.5$  GeV, we find a much flatter spectrum, with  $a = 2.78 \pm 0.28$ .

The  $x_F$ -distribution for  $\bar{p}$ -induced  $J/\psi$  events is shown in Fig. 6, where the data from proton and  $\pi^-$  beams are also shown for comparison. We conclude that the  $\bar{p}$ -induced spectrum closely resembles that of protons, and is inconsistent with that of  $\pi^-$ -induced events.

Parametrizations of  $d\sigma/dx_F$  are given in Table I.

(c) Dependence on  $p_T$

A typical relative cross section  $\frac{1}{p} \frac{d\sigma}{dp_T}$  is shown in Fig. 7. (The acceptance of the spectrometer extends well beyond the highest  $p_T$ 's observed.) Within the precision of the experiment the data are consistent with an exponential falloff except in the region of  $p_T < 1$  GeV/c. In Fig. 8, the mean transverse momenta for  $\pi^-$ -induced events with  $x_F > 0$  are plotted versus pair mass, correction having been made for the efficiency. Data at lower masses from our previous work<sup>1</sup> are shown for comparison. The mean  $p_T$  increases with mass up to  $M \approx 4$  GeV, where it reaches a plateau value of approximately 1.2 GeV/c. Also shown in the figure are the CFS results<sup>3</sup> for  $x_F = 0$  pairs produced with a 200 GeV/c proton beam. A similar plateau is seen, but at a value 200 MeV/c lower. Proton-induced data from our experiment also exhibit a lower  $\langle p_T \rangle$  at  $M \approx 4$  GeV. These results are summarized in Table II, along with measurements of  $\langle p_T^2 \rangle$  for the various particle types and mass intervals.

To test if the difference in  $\langle p_T \rangle$  between protons and pions is due to a variation in  $\langle p_T \rangle$  with  $x_F$ , in Fig. 9 we have plotted  $\langle p_T \rangle$  versus  $x_F$  for several intervals of pair mass. Within uncertainties of  $\approx 100$  MeV/c, no variation of  $\langle p_T \rangle$  with  $x_F$  is observed.

(d) Dependence on Helicity Angle

Careful measurements of the cross section  $d\sigma/d(\cos\theta^*)$  were made to search for alignment of the dimuon spin. Because the choice of polar axis is strongly motivated by the Drell-Yan model, we defer discussion of this aspect of the data to a later section.

(e) Dependence on Atomic Mass Number of the Target

Previous measurements<sup>1,4</sup> have shown that the cross sections for  $\mu$ -pair production are consistent with a power law  $\sigma(A) = \sigma_0 A^\alpha$  (1) where  $\sigma_0$  is the free nucleon cross section and  $A$  the atomic mass number of the target nucleus. The power  $\alpha$  increases from approximately 2/3 at the lowest masses, to a value close to unity as  $M$  increases above  $\approx 2$  GeV. For proton-induced pairs, the data<sup>5,6</sup> are consistent with  $\alpha=1$  throughout the mass range 4-12 GeV. This experiment gives the first measurements of  $\alpha$  in  $\pi^-$  events above the 4 GeV pair mass.

Results on  $A$  dependence have already been reported by other groups<sup>7</sup> for single hadron production as a function of  $p_T$  at  $x_F=0$ . They find an exponent  $\alpha$  which increases with  $p_T$  to a plateau value of 1.15 to 1.3 depending on the particle mass. The plateau value is reached at  $p_T \sim 5$  GeV/c. These observations have prompted considerable theoretical discussion.<sup>8</sup> It is then interesting to inquire whether the  $\mu$ -pair continuum shows a similar  $A$  dependence versus  $p_T$  and how this compares with  $J/\psi$  production.

Figure 10 shows the  $p_T$  variation of  $\alpha$  for three different intervals of  $M_{\mu\mu}$ . One interval is the continuum below the  $J/\psi$  ( $2.0 < M_{\mu\mu} < 2.7$  GeV/c<sup>2</sup>). One shows the  $J/\psi$  itself, ( $2.7 < M_{\mu\mu} < 3.5$  GeV/c<sup>2</sup>), and one is for the continuum above the  $J/\psi$  ( $M_{\mu\mu} > 4$  GeV/c<sup>2</sup>). A systematic increase of  $\alpha$  with  $p_T$  is seen in the  $J/\psi$  interval. Since these data are integrated over all  $x_F$  it is important to investigate whether certain regions of  $x_F$  produce a rise in  $\alpha$ . Figure 11 shows the  $x_F$  dependence of  $\alpha$  for the same mass intervals. No significant increase in  $\alpha$  is seen in any  $x_F$  interval.

The mass dependence of  $\alpha$  is shown in Fig. 12. The power of  $\alpha$  rises to  $1.19 \pm 0.10$  at a mass of 7.2 GeV/c<sup>2</sup>. The statistical error associated with each cross section has been combined in quadrature with a 12% systematic error. In each mass interval the least squares fit to the form  $\sigma = \sigma_0 A^\alpha$  gives a good  $\chi^2$ .



### III. Quark-Antiquark Annihilation and $\pi^+/p$ , $\pi^+/\pi^-$ Cross Section Ratios

It is useful to have a theoretical framework to describe several features of the data. The general formalism of lepton pair production by hadrons has been discussed in detail by Lam and Tung.<sup>9</sup> An important special case is the description in terms of quark-antiquark annihilation to produce a lepton pair through an intermediate virtual photon. This so-called Drell-Yan mechanism has been extensively discussed in the literature.<sup>10</sup> The  $\mu$ -pair production cross section for interacting hadrons A and B, neglecting  $p_T$ , is:<sup>11</sup>

$$\frac{d\sigma}{dM dx_F} = \frac{8\pi\alpha^2}{9M^3} \sum_i \frac{e_i^2}{(x_1+x_2)} [x_1 f_i^A(x_1) x_2 f_{\bar{i}}^B(x_2) + x_1 f_{\bar{i}}^A(x_1) x_2 f_i^B(x_2)] \quad (1)$$

where  $x_{1,2} = \frac{1}{2} (\pm x_F + \sqrt{x_F^2 + 4M^2/s})$  are the momentum fractions (Feynman-x) of the annihilating quarks in the projectile and target hadrons,

$x f_i^A(x)$  is the momentum spectrum for quarks of flavor  $i$  in hadron A.

Thus, the observed mass and Feynman-x spectra for the data reflect the distributions of the annihilating quarks.

Consider first the predictions of this mechanism for lepton pair production in nucleon-nucleon and pion nucleon scattering. In the case of nucleon-nucleon scattering the interacting particles contain no valence antiquarks and only antiquarks from the  $q\bar{q}$  sea can contribute. Since the probability density functions for the sea quarks fall steeply with  $x_1$  and  $x_2$  the observed mass spectrum should fall rapidly with mass for fixed  $x_F$ . Incident pions, on the other hand, contain a valence antiquark which has a significant probability of being found at large  $x_1$ . Thus the mass spectrum for pion induced pairs should fall more slowly with mass than for incident protons.

Figure 13 shows the cross section ratio of pion production to proton production as a function of mass. Cross sections at  $y=0$  ( $x_F=0$ ) are used to permit, for the highest mass points, comparison of our pion measurements with proton induced data from other experiments.<sup>3</sup> The pion to proton ratio rises to 270 at  $M/\sqrt{s}$  of 0.52 in dramatic agreement with the expected trend.

Consider next the comparison of the  $\pi^+$  and  $\pi^-$ -induced  $\mu$ -pair production cross sections. In this case, valence quarks and antiquarks from the interacting particles should dominate production for large values of  $x_1$  and  $x_2$ . In this experiment a carbon target was used so that the target is exactly symmetric in u and d quark distributions ( $u^p=d^n, d^p=u^n$ ). In the case of an incident  $\pi^-$  the valence antiquark is a  $\bar{u}$  with charge 2/3 while for an incident  $\pi^+$  it is a  $\bar{d}$  with charge 1/3. Since the pair production varies like the square of the quark charge, one expects  $\sigma(\pi^+C \rightarrow \mu^+\mu^- \dots)/\sigma(\pi^-C \rightarrow \mu^+\mu^- \dots)$  to be 1/4. If  $x_1$  and  $x_2$  are not both large, sea antiquarks can contribute and the cross section ratio approaches 1 as  $x_1, x_2$  approach 0. Figure 14 shows the measured  $\pi^+/\pi^-$  cross section ratio as a function of pair mass. It is seen to be unity for the  $J/\psi$  as might be expected for strong production from charge symmetric initial states. The data correspond to  $x_F > 0$ . As the pair mass increases above 3.1 GeV/c<sup>2</sup> the ratio falls toward 1/4 as expected.

#### IV. Helicity Angular Distributions

Two variables, in addition to  $M$ ,  $x_F$ ,  $p_T$ , are required to specify the  $\mu$ -pair final state. A natural choice are the polar and azimuthal angles of one of the muons in the  $\mu$ -pair rest frame. The polar, or helicity angle, can be specified with respect to several available directions. Figure 15 shows the four reference directions we have investigated. The s-channel system uses the vector of the recoil system. The t-channel uses the beam direction. The u-channel uses the target particle direction and the Collins-Soper system<sup>12</sup> uses a vector which bisects the angle between the beam and the reverse of the target vector. It should be noted that if the  $p_T$  of the final state  $\mu$ -pair is zero all four of these directions are equivalent.

The annihilation of two spin-1/2 fermions to a  $1^-$  intermediate state leads to a  $1+\cos^2\theta^*$  distribution for the final state lepton pair. This is the case of the simple Drell-Yan mechanism. Since the observed  $\mu$ -pairs do have transverse momenta the  $q\bar{q}$  direction in the  $\mu$ -pair cm system cannot be uniquely determined. The Collins-Soper vector is the best estimate of that direction in the context of the quark-parton model.

We have examined the distribution of these four helicity angles for three different mass regions, below the  $J/\psi$  ( $2.0 < M < 2.7$  GeV), the  $J/\psi$  ( $2.7 < M < 3.5$ ), and above the  $J/\psi$  ( $M > 3.5$ ). These distributions are shown in Fig. 16 with their best fits to the form  $1+\alpha\cos^2\theta^*$ . Results of the fits are given in Table III. It should be noted that variation of acceptance with angle is not the same for all four angles. Results for the angular distribution at the  $J/\psi$  are consistent with a flat distribution except for the t-channel angle which shows a coefficient of  $\cos^2\theta^*$  of  $0.33 \pm 0.06$ .

Strong evidence for a  $\cos^2\theta^*$  term is seen in the continuum both above and below the  $J/\psi$ . The detector efficiency as a function of angle is not strongly mass dependent so that the change of these distributions with mass reflects a clear change in the underlying production mechanism.

A number of attempts have been made to explain the broad  $p_T$  spectra for the  $\mu$ -pairs in terms of QCD corrections to the Drell-Yan mechanism.<sup>13</sup> The corrections are expected to be most significant at higher  $p_T$ . We have investigated these helicity angular distributions for transverse momenta above and below 1 GeV/c. Results are shown in Fig. 17. Evidence for spin alignment is seen in both  $p_T$  intervals.

#### V. Factorization and the Pion Structure Function

A further test of the  $q\bar{q}$  annihilation mechanism is possible for large values of  $x_1$ . If  $x_1$  is large enough so that sea quarks contribute negligibly to the pair production then, using the relation  $x\bar{u}^\pi(x) = x d^\pi(x)$  and setting terms involving the pion sea distributions to zero, equation (1) becomes

$$\frac{d\sigma}{dM dx_F} = \frac{8\pi\alpha^2}{9M^3(x_1+x_2)} x_1 \bar{u}^\pi(x_1) \left[ \frac{4}{9} x_2 u^N(x_2) + \frac{1}{9} x_2 \bar{d}^N(x_2) \right] \text{ (for } \pi^- N \text{)}$$

(2)

$$\text{or } M^2 \frac{d\sigma}{dx_1 dx_2} = \frac{4\pi\alpha^2 s}{9} x_1 \bar{u}^\pi(x_1) \cdot \left[ \frac{4}{9} x_2 u^N(x_2) + \frac{1}{9} x_2 \bar{d}^N(x_2) \right].$$

Since  $M^2/s = x_1 x_2$  the cross section as a function of  $x_1$  and  $x_2$  is predicted to factor into a function of  $x_1$  times a function of  $x_2$ . The form of equation (2) is used to test the factorization hypothesis and to deduce the functions of  $x_1$  and  $x_2$  which are the pion structure function and a linear combination of two nucleon quark distribution functions.

To use equation (2), data with  $x_1 > 0.2$ ,  $M > 4 \text{ GeV}/c^2$ ,  $x_F > 0$  are binned in a rectangular grid of  $x_1$  and  $x_2$ . Events are corrected for efficiency and weighted by  $M^4$ . The range of  $x_1$  in this sample is 0.2 to 1 and  $x_2$  is 0.05 to 0.27. The distribution of events in the  $x_1, x_2$  plane is shown in Fig. 18 together with the kinematic relations  $x_F = x_1 - x_2$  and  $M^2/s = x_1 x_2$ .

To test the factorization hypothesis a grid of 141 populated bins in the  $x_1, x_2$  plane, representing  $M^4 d\sigma/dx_1 dx_2$  is fit by 16 values representing the pion function versus  $x_1$  and 12 values representing the nucleon function versus  $x_2$ . We find a  $\chi^2$  of 133 for the 113 degrees of freedom indicating a reasonable agreement with the factorization hypothesis especially since no allowance for systematic uncertainty has been made in the error estimates entering the  $\chi^2$ . Thus, once again, the data are in good agreement with an expected feature of the quark annihilation mechanism.

To deduce the pion structure function the shape determined in the factorization test must be suitably normalized. Only the normalization of the product of the pion and nucleon functions is measured directly. To set the normalization, the nucleon function is compared with expectations based on deep inelastic lepton scattering data and fits to these data which include the  $q^2$  dependence expected from QCD.<sup>14</sup> In this comparison we use  $q^2 = M^2$ . The nucleon function deduced from this experiment is normalized to the expected function over the interval  $0.05 < x_2 < 0.27$ .

The resulting pion structure function is shown in Fig. 19 and the nucleon function is given in Fig. 20 together with the expected shape. The agreement of the latter is not good. It should be noted that very little lepton scattering data are available to constrain the QCD fits in the range  $q^2 > 16 \text{ GeV}^2$ . Moreover, the nucleon function is rather sensitive to such

effects as  $p_T$  and mass of the annihilating quarks and to Fermi motion. The poor agreement shown in Fig. 20 indicates that the normalization of the pion function should be used with caution. This normalization question will be a problem for all lepton pair experiments until the deep inelastic lepton scattering data improves and until there is a more complete theoretical understanding of how to include quark mass and  $p_T$  effects.

The shape of the pion function has been fit to the form  $(1-x)^a$  and the value  $a = 1.05 \pm 0.06$  is obtained, where the error is purely statistical. The quark counting rules of Brodsky and Farrar<sup>15</sup> predict the form  $(1-x)^1$  for the pion valence quarks, in excellent agreement with our measurement.

Since the definition of  $x_1$  and  $x_2$  used to determine the structure functions given above neglects the  $p_T$  of the  $\mu$ -pair, we have tried to estimate the influence of non-zero  $p_T$ . There is no unique way to incorporate the observed  $p_T$  since its origin is unknown. If it arises from the intrinsic  $p_T$  of the annihilating quarks then only the vector sum of the two quark transverse momenta is measured and the true  $x_1$  and  $x_2$  values cannot be determined.

Two prescriptions for including  $p_T$  effects have been tried. In the first, the quarks are assumed to have a fixed  $p_T$  of 1 GeV/c and the angle between their  $p_T$  vectors is chosen to produce the observed transverse momentum for pairs with  $p_T < 2$  GeV/c. This treatment leads to a negligible change in the pion structure function but the nucleon function is flattened rather strongly. A fit to the nucleon function with the form  $(1-x)^a$  yields  $a = 5.7$  with no  $p_T$  compensation and 2.2 with compensation.

An alternate treatment is to assume that the  $p_T$  vectors of the quark and antiquark are always aligned and equal. This prescription leads to somewhat larger changes in the pion function. The power of the  $(1-x)^a$  fit changes upward by about 0.2.

Using the normalization discussed above we find

$$\int_{0.25}^1 \bar{u}^{\pi^-}(x) dx = 0.25$$

$$\int_{0.25}^1 x \bar{u}^{\pi^-}(x) dx = 0.11$$

Since both valence quarks in the pion have the same distribution function, the first integral indicates that the probability of finding a valence quark in the pion with  $x$  greater than 0.25 is 50%. The second integral indicates that only 22% of the pion momentum is carried by valence quarks in this interval.

In conclusion, this experiment has observed several rather striking predictions of the  $q\bar{q}$  annihilation model such as the mass dependence of the  $\pi^-/p$  and  $\pi^+/\pi^-$  cross section ratios, evidence for spin alignment of the  $\mu$ -pair system and factorization of the cross section. The pion structure function has been determined in the context of this annihilation mechanism.

#### Acknowledgements

We are pleased to acknowledge the CERN-Heidelberg group and in particular Jack Steinberger for the loan of the large multiwire proportional chambers used in the upstream part of the spectrometer. We thank Val Fitch for the use of one of the beam Cerenkov counters. Excellent engineering support was received from Richard Armstrong and Howard Edwards and their staffs at Chicago and Princeton. The Fermilab Neutrino Department greatly facilitated the installation and operation of the detector. John Zerolis was especially helpful in detector testing and in setting up an event scanning facility.

## References

- \* Work performed at the Fermi National Accelerator Laboratory and supported in part by the Energy Research and Development Administration and the National Science Foundation.
- † Present address: Los Alamos Scientific Laboratory.
1. J. G. Branson et al., Phys. Rev. Letters 38, 1334 (1977), and references contained therein.
  2. K. J. Anderson et al., submitted to Physical Review; J. G. Branson, Ph.D. Thesis, Princeton University, Princeton, New Jersey, 1977 (unpublished).
  3. R. D. Kephart, Vanderbilt Conference, Nashville, Tennessee, 1978 (unpublished).
  4. M. Binkley et al., Phys. Rev. Letters 37, 571 (1976).
  5. D. M. Kaplan et al., Phys. Rev. Letters 40, 435 (1978).
  6. D. Antreasyan et al., Phys. Rev. Letters 39, 906 (1977).
  7. J. W. Cronin et al., Phys. Rev. D11, 3105 (1975); and references contained therein; U. Becker et al., Phys. Rev. Letters 37, 1731 (1976); L. Kluberg et al., Phys. Rev. Letters 38, 670 (1977).
  8. See, for example, references 4-12 of L. Kluberg et al., Ref. 7.
  9. C. S. Lam and Mu-Ki Tung, A Systematic Approach to Inclusive Lepton Pair Production in Hadronic Collisions, McGill University, Department of Physics preprint.
  10. See, for example, G. R. Farrar, Nuclear Physics B77, 429 (1974) and references contained therein.
  11. The appropriate definition of  $x_F$  for the  $q\bar{q}$  annihilation model is  $x_F = 2p_{||}^* / \sqrt{s}$ . The definitions of  $x_1, x_2$  in terms of  $x_F, M$  given with equation (1) use this definition.



- 
12. J. C. Collins and D. E. Soper, Phys. Rev. D16, 2219 (1977).
  13. C. T. Sachrajda, Phys. Lett. 73B, 185 (1978); G. Altarelli, G. Parisi and R. Petronzio, CERN preprints TH-2413 (1977) and TH-2450 (1978).
  14. A. J. Buras and K.J.F. Gaemers, Nuclear Physics B132, 249 (1978).
  15. S. J. Brodsky and G. R. Farrar, Phys. Rev. Letters 31, 1153 (1973).

---

TABLE CAPTIONS

Table I      The dependence of the  $\mu$ -pair cross section on  $x_F$   
for various incident particles and mass intervals.

Table II     Mean  $p_T$  and  $p_T^2$  for various incident particles and  
kinematic intervals.

Table III    Results of fits to the helicity angular distribution.

TABLE I

$x_F$ Dependence Fits to $\frac{d\sigma}{dx_F} \sim (1-x_F)^b$	
$\pi^- N \rightarrow \mu^+ \mu^- X$	
Mass Interval (GeV/c <sup>2</sup> )	b
J/ $\psi$	1.99 $\pm$ .05
3.5- 4.5	1.32 $\pm$ .05
4.5- 6.5	0.91 $\pm$ .06
6.5- 8.5	0.68 $\pm$ .10
8.5-12.0	0.40 $\pm$ .17
$\bar{p} N \rightarrow \mu^+ \mu^- X$	
J/ $\psi$	3.90 $\pm$ .40
$\pi^+ C \rightarrow \mu^+ \mu^- X$	
J/ $\psi$	2.20 $\pm$ .06
3.5- 4.5	1.37 $\pm$ .13
$p C \rightarrow \mu^+ \mu^- X$	
J/ $\psi$	4.30 $\pm$ .10
3.5- 4.5	2.78 $\pm$ .28

TABLE II

Mean Transverse Momentum and Mean Transverse Momentum Squared  
Versus Muon Pair Mass and Beam Particle Type

Mass (GeV/c)	$\langle p_T \rangle$ (GeV/c)			
	BEAM PARTICLE TYPE			
	p	$\bar{p}$	$\pi^+$	$\pi^-$
2.0- 2.7	.79 $\pm$ .10	1.17 $\pm$ .34	.82 $\pm$ .10	.82 $\pm$ .10
J/ $\psi$	.97 $\pm$ .01	.88 $\pm$ .13	1.01 $\pm$ .10	1.05 $\pm$ .10
3.5- 4.5	1.00 $\pm$ .13	1.26 $\pm$ .49	1.05 $\pm$ .12	1.10 $\pm$ .10
4.5- 6.5	.87 $\pm$ .21	--	1.16 $\pm$ .25	1.25 $\pm$ .10
6.5- 8.5	--	--	1.08 $\pm$ .45	1.17 $\pm$ .12
8.5-12.0	--	--	--	1.17 $\pm$ .16
Mass (GeV/c)	$\langle p_T^2 \rangle$ (GeV <sup>2</sup> /c <sup>2</sup> )			
	BEAM PARTICLE TYPE			
	p	$\bar{p}$	$\pi^+$	$\pi^-$
2.0- 2.7	.81 $\pm$ .10	1.80 $\pm$ .50	.87 $\pm$ .10	.89 $\pm$ .10
J/ $\psi$	1.25 $\pm$ .10	1.02 $\pm$ .14	1.33 $\pm$ .10	1.47 $\pm$ .10
3.5- 4.5	1.42 $\pm$ .15	1.70 $\pm$ .70	1.47 $\pm$ .14	1.64 $\pm$ .10
4.5- 6.5	.91 $\pm$ .20	--	1.63 $\pm$ .34	2.06 $\pm$ .11
6.5- 8.5	--	--	1.56 $\pm$ .65	1.79 $\pm$ .15
8.5-12.0	--	--	--	1.57 $\pm$ .20

TABLE III

## Helicity Angular Distribution Fits

$2.0 < M_{\mu\mu} < 2.6 \text{ GeV}/c^2$				
Angle	Flat $\chi^2/DF$	$1+\cos^2\theta^*$ $\chi^2/DF$	$1+\alpha\cos^2\theta^*$ $\alpha$	$\chi^2/DF$
s channel	77.5/9	15.7/9	$1.10 \pm .11$	15.3/8
t channel	67.4/9	15.7/9	$.71 \pm .11$	8.8/8
u channel	102.5/9	34.2/9	$1.72 \pm .22$	22.4/8
Collins-Soper	79.7/9	25.6/9	$1.14 \pm .17$	25.0/8
$J/\psi$				
s channel	19.0/9	240.0/9	$.03 \pm .04$	18.7/8
t channel	36.7/9	101.0/9	$.33 \pm .06$	2.2/8
u channel	12.3/9	131.0/9	$.09 \pm .06$	10.7/8
Collins-Soper	7.0/9	212.0/9	$-.10 \pm .05$	4.7/8
$M_{\mu\mu} > 3.5 \text{ GeV}/c^2$		All $p_T$		
s channel	32.3/9	104.0/9	$.05 \pm .09$	32.0/8
t channel	49.7/9	11.1/9	$.82 \pm .15$	9.8/8
u channel	47.8/9	17.7/9	$1.31 \pm .26$	16.2/8
Collins-Soper	44.6/9	6.6/9	$1.30 \pm .23$	4.9/8
$M_{\mu\mu} > 3.5 \text{ GeV}/c^2$		$p_T > 1.0 \text{ GeV}/c$		
s channel	11.7/7	25.4/7	$.16 \pm .19$	11.0/6
t channel	30.4/9	15.8/9	$.65 \pm .17$	12.4/8
u channel	29.4/7	13.7/7	$1.42 \pm .39$	12.5/6
Collins-Soper	36.4/9	11.2/9	$1.47 \pm .39$	8.8/8
$M_{\mu\mu} > 3.5 \text{ GeV}/c^2$		$p_T < 1.0 \text{ GeV}/c$		
s channel	13.1/7	11.9/7	$.50 \pm .22$	7.4/6
t channel	26.0/9	3.3/9	$1.05 \pm .24$	3.3/8
u channel	28.2/9	12.6/9	$1.11 \pm .31$	12.5/8
Collins-Soper	31.6/9	12.6/9	$1.17 \pm .29$	12.2/8

## FIGURE CAPTIONS

- Fig. 1 Plan view of the spectrometer.
- Fig. 2 Use of hodoscope information to calculate the mass of the muon pair.
- Fig. 3 Differential cross section versus mass, for  $\pi^-$ -induced events.  
Data from C, Cu, and W targets have been combined.
- Fig. 4 Differential cross section  $d\sigma/dM$  for the mass range  $2 < M < 5$  GeV.  
The solid line is a fit to  $J/\psi$  and  $\psi'$  gaussians with widths  
140 MeV/c<sup>2</sup>, and an exponentially decreasing continuum.
- Fig. 5 Relative cross section  $d\sigma/dx_F$  versus  $x_F$  for different mass intervals.  
The abscissa is defined in the text.
- (a)  $\pi^-$ -induced events on nuclear targets.
  - (b) Proton-induced events on a carbon target.
- Fig. 6 Relative cross section  $d\sigma/dx$  for  $\bar{p}$ -induced  $J/\psi$  events on a carbon  
target. Curves for proton and  $\pi^-$ -induced events are shown for  
comparison.
- Fig. 7 Differential cross section  $1/p_T d\sigma/dp_T$  for  $\pi^-$ -induced events at  
the  $J/\psi$  mass and in the region  $4.5 < M < 6.5$  GeV.
- Fig. 8 The mean transverse momentum (corrected for spectrometer  
acceptance) versus pair mass  $M$ .
- Fig. 9 The mean transverse momenta of  $\pi^-$ -induced events are plotted versus  
 $x_F$  for several intervals of pair mass.

- Fig. 10 The A dependence of  $\pi^-$ -induced  $\mu$ -pair production is studied as a function of  $p_T$ . The power  $\alpha$  (see text) is plotted, for three mass intervals, versus  $p_T$  of the pairs.
- Fig. 11 The power  $\alpha$  is plotted versus  $x_F$  for three mass intervals, for  $\pi^-$ -induced events.
- Fig. 12 The power  $\alpha$  is shown as a function of pair mass  $M$ , for  $\pi^-$ -induced events.
- Fig. 13 The ratio of  $\pi^-$ -induced to proton-induced  $\mu$ -pair cross section at  $y=0$  as a function of  $M/\sqrt{s}$ .
- Fig. 14 The ratio of  $\pi^+$ -induced to  $\pi^-$ -induced  $\mu$ -pair cross section for  $x_F > 0$  as a function of mass.
- Fig. 15 Reference directions for measuring the helicity angle of the  $\mu$ -pair in the pair rest frame.
- Fig. 16 Helicity angular distributions for the four reference directions in three different mass intervals. The data are  $\pi^-$ -induced events with  $x_F > 0$  and all  $p_T$ .
- Fig. 17 Helicity angular distributions for data with  $M > 3.5$  GeV in two intervals of  $p_T$ .
- Fig. 18 The kinematic relations between  $x_1$ ,  $x_2$  and  $x_F$ ,  $M$ . The points show the distribution of events used for the structure function analysis.

Fig. 19      The pion structure function  $x\bar{u}(x)$  measured with incident  $\pi^-$  mesons on copper and tungsten targets.

Fig. 20      The nucleon function  $\frac{4}{9} xu^N(x) + \frac{1}{9} xd^N(x)$  averaged over protons and neutrons in the target. The comparison curve is based on deep inelastic lepton scattering data and QCD scale breaking predictions of Ref. 14.



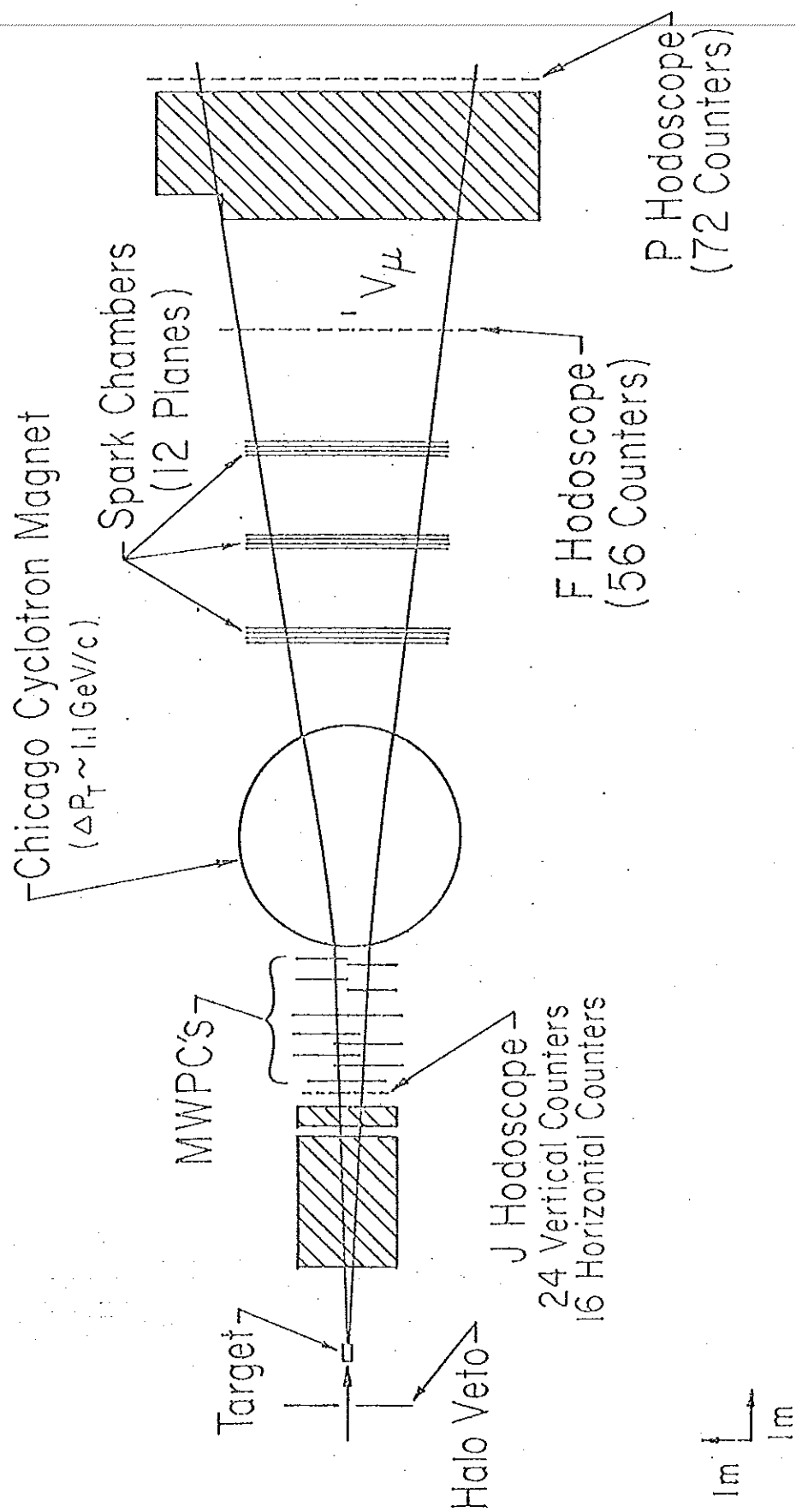


Fig. 1

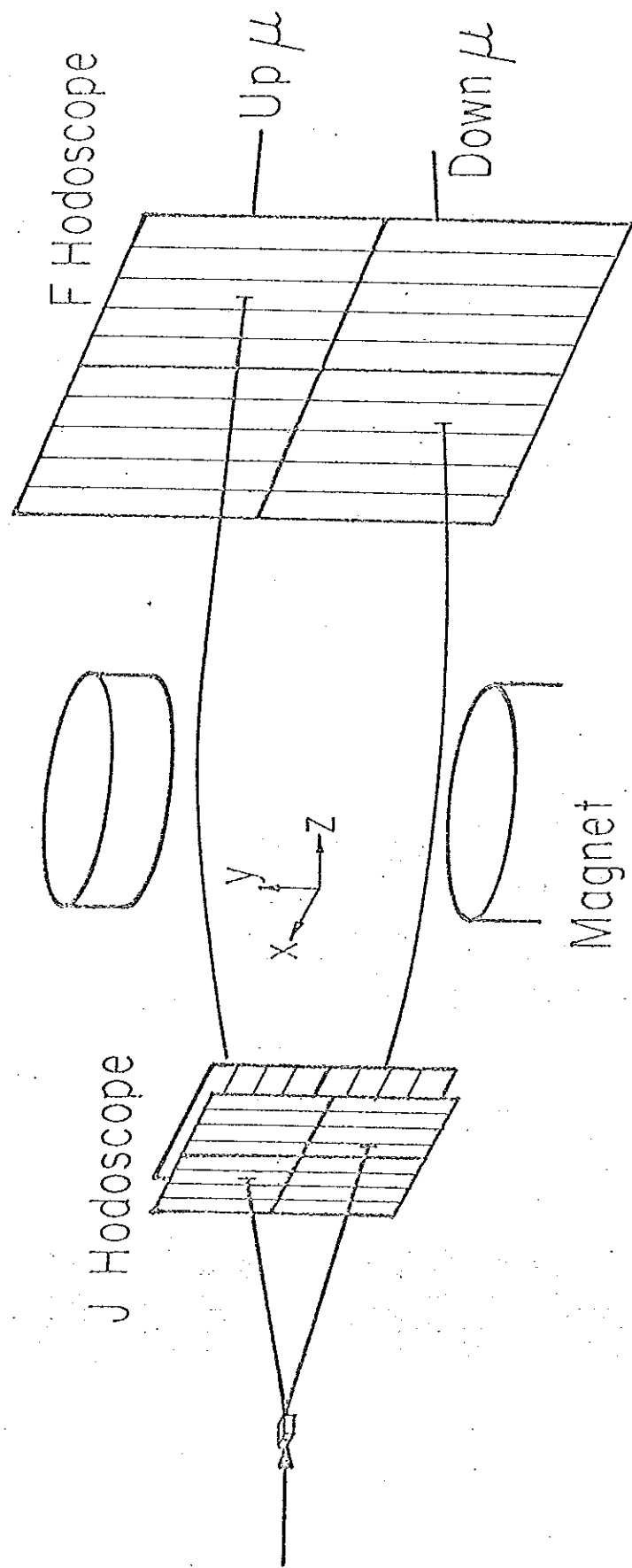


Fig. 2

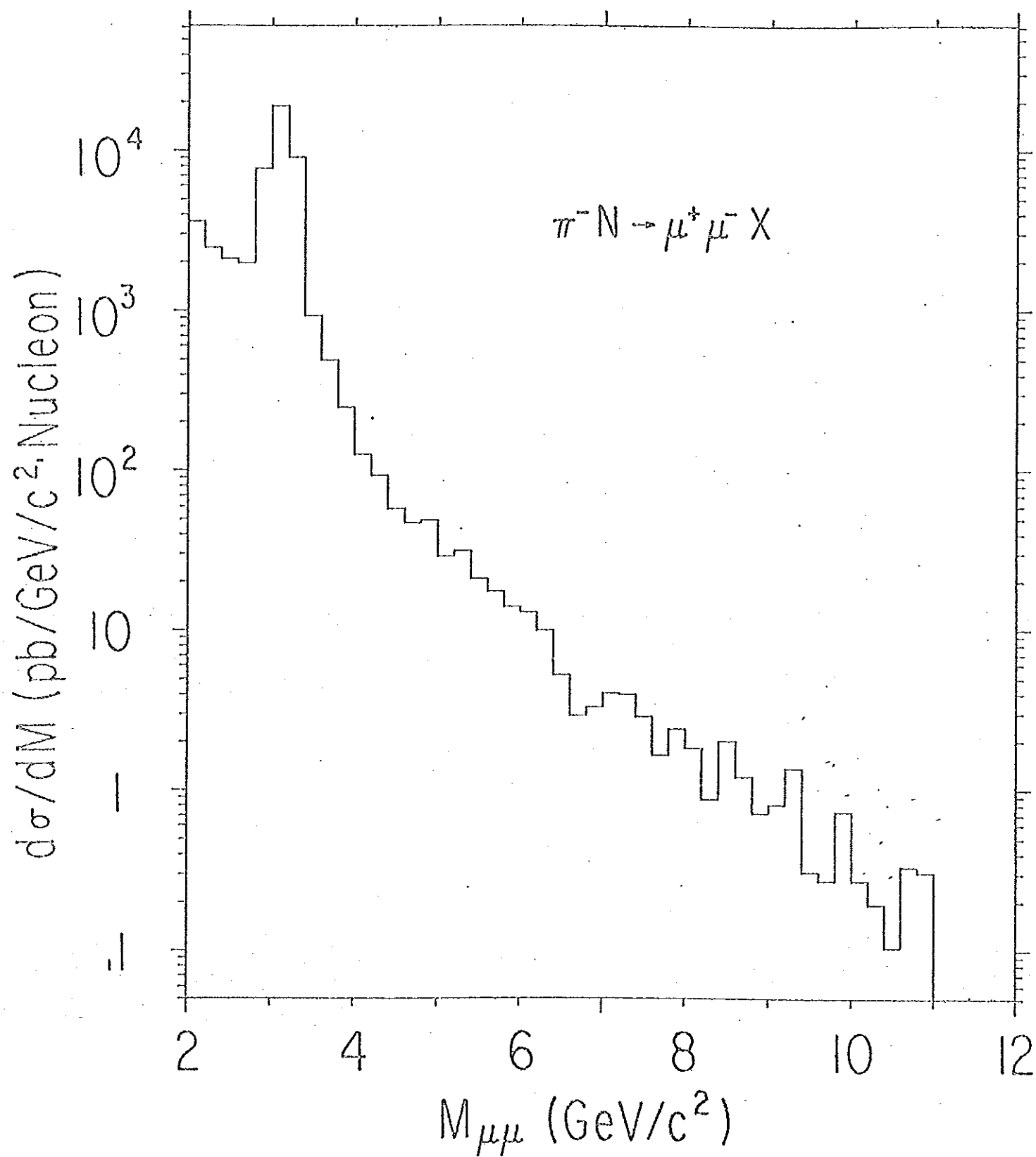


Fig. 3

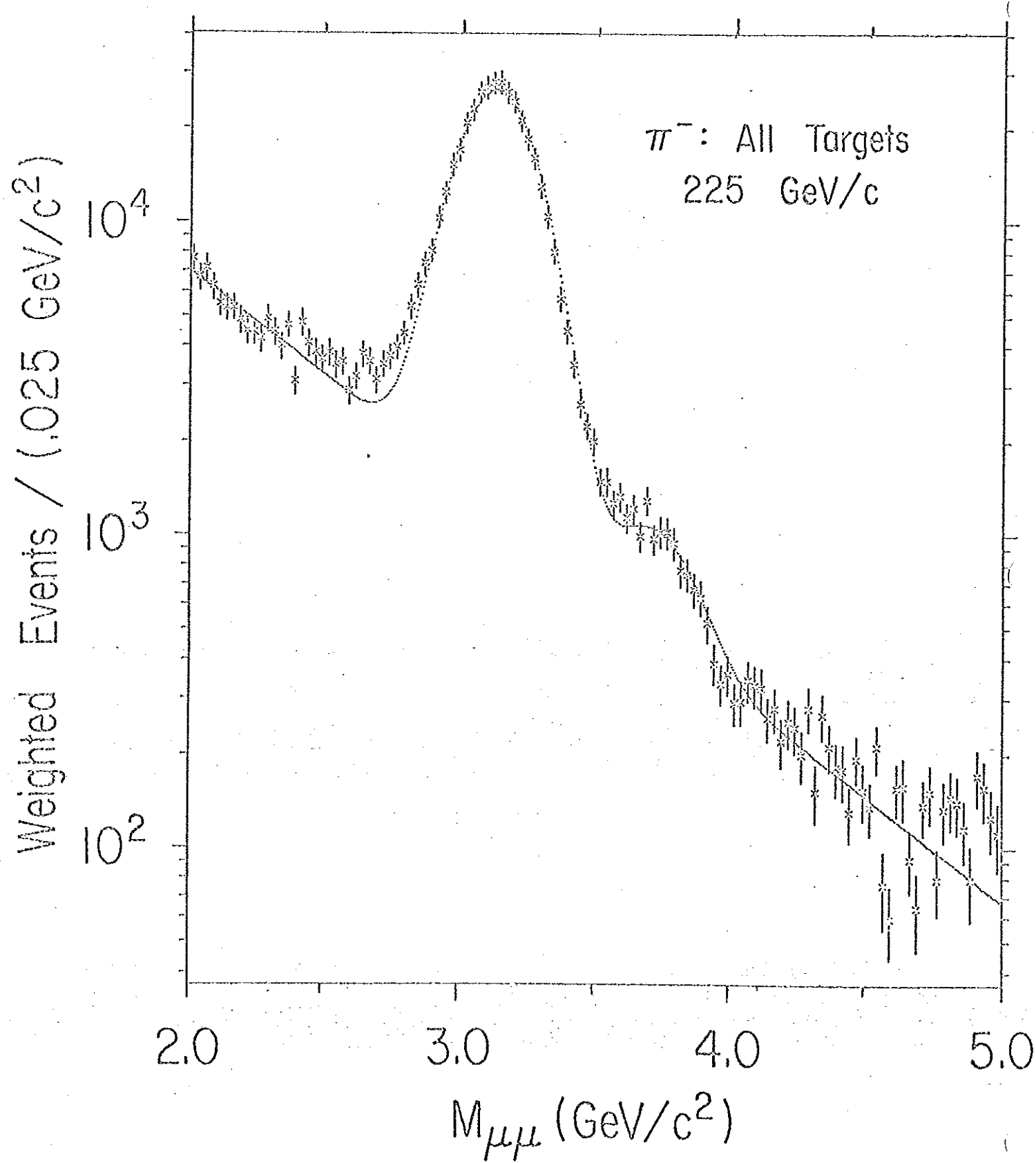


Fig. 4

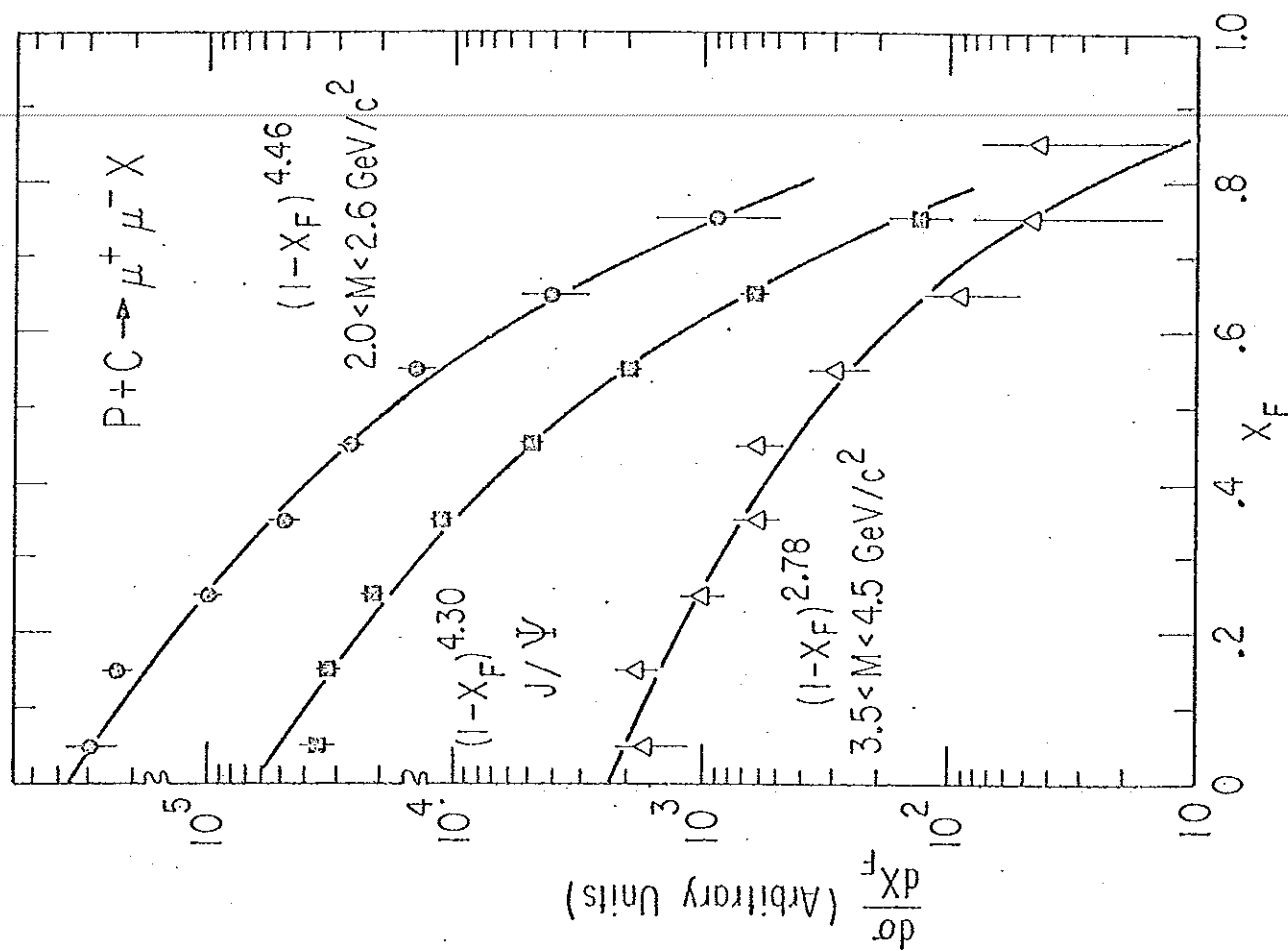
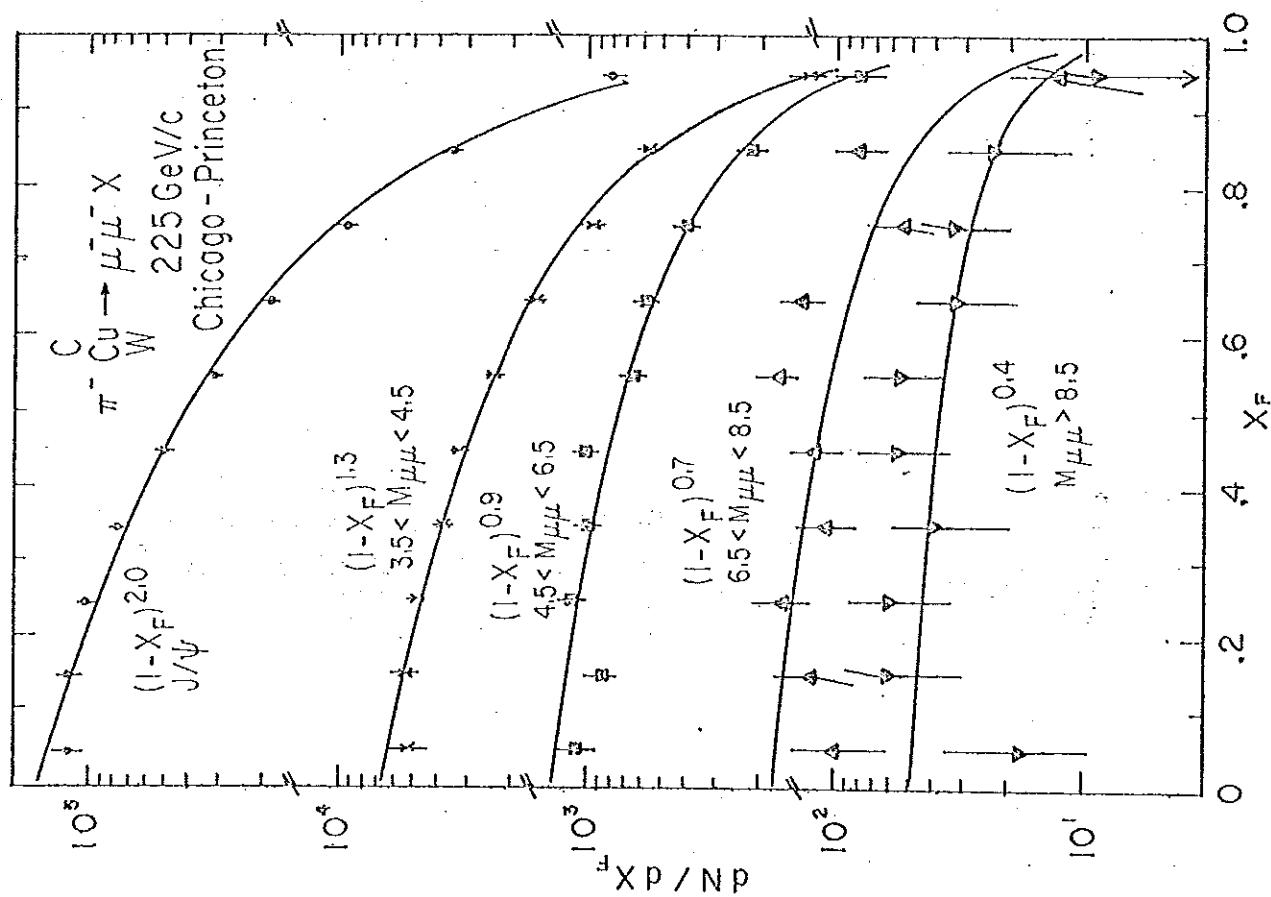


Fig. 5 a - b

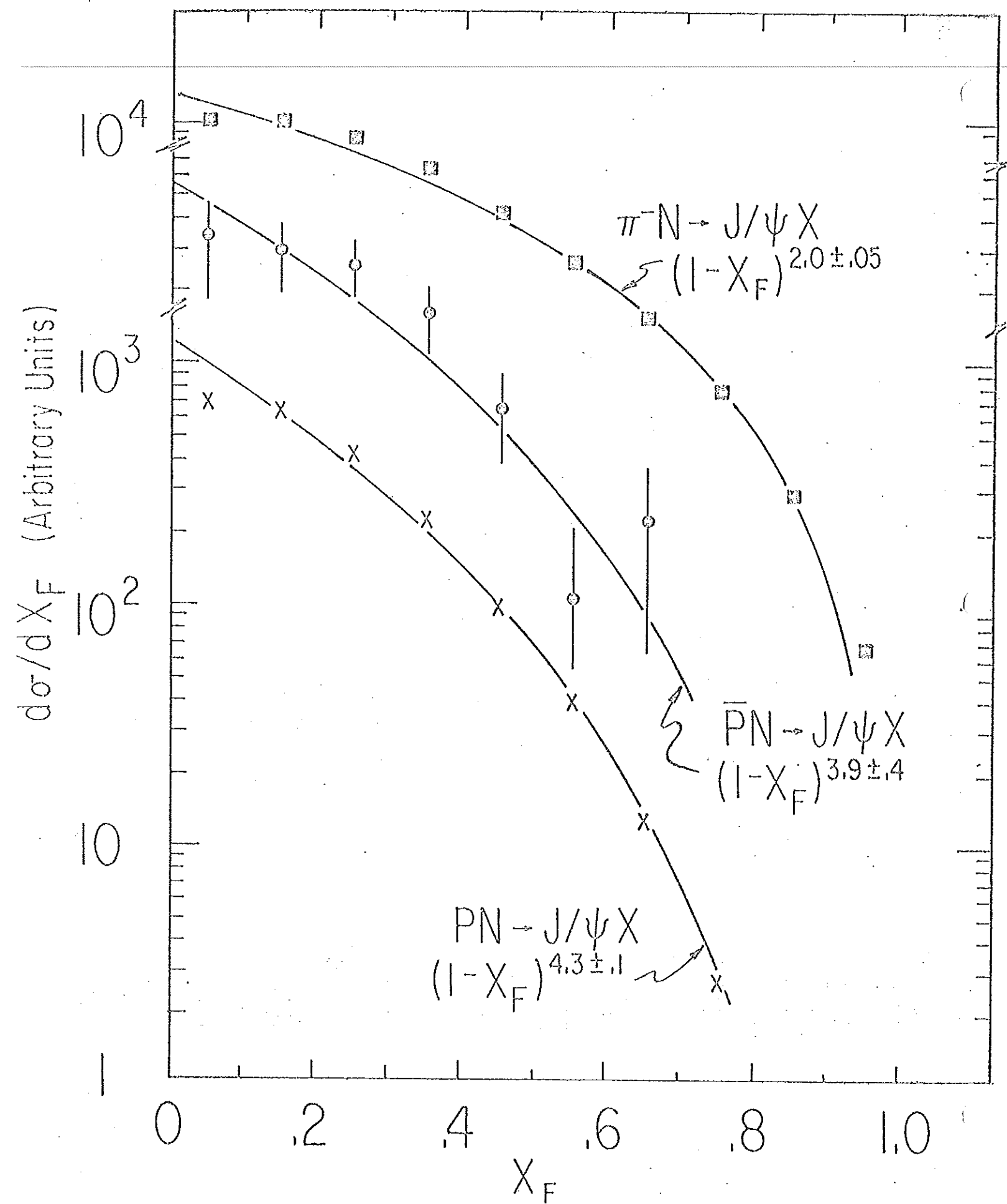


Fig. 6

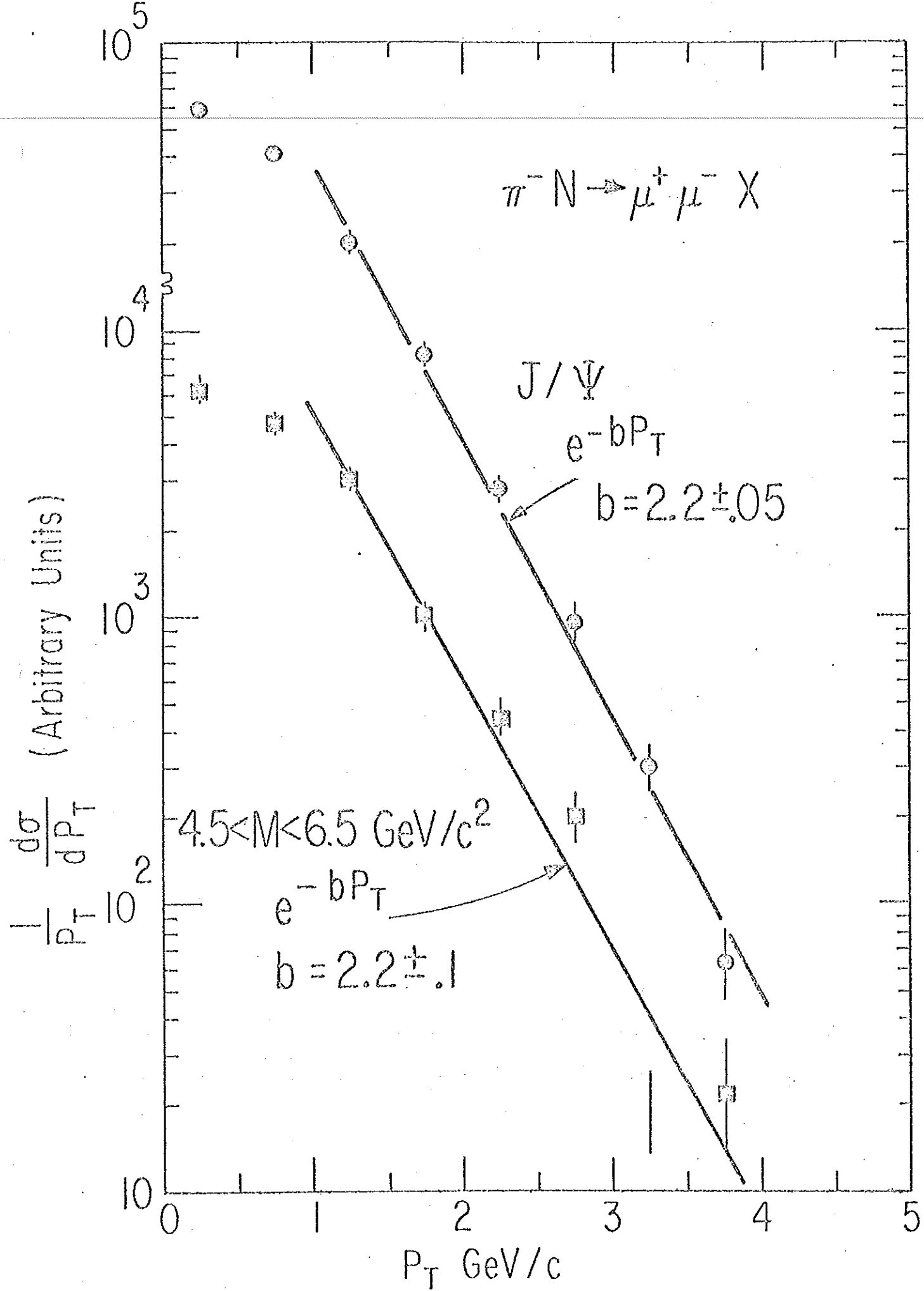


Fig. 7

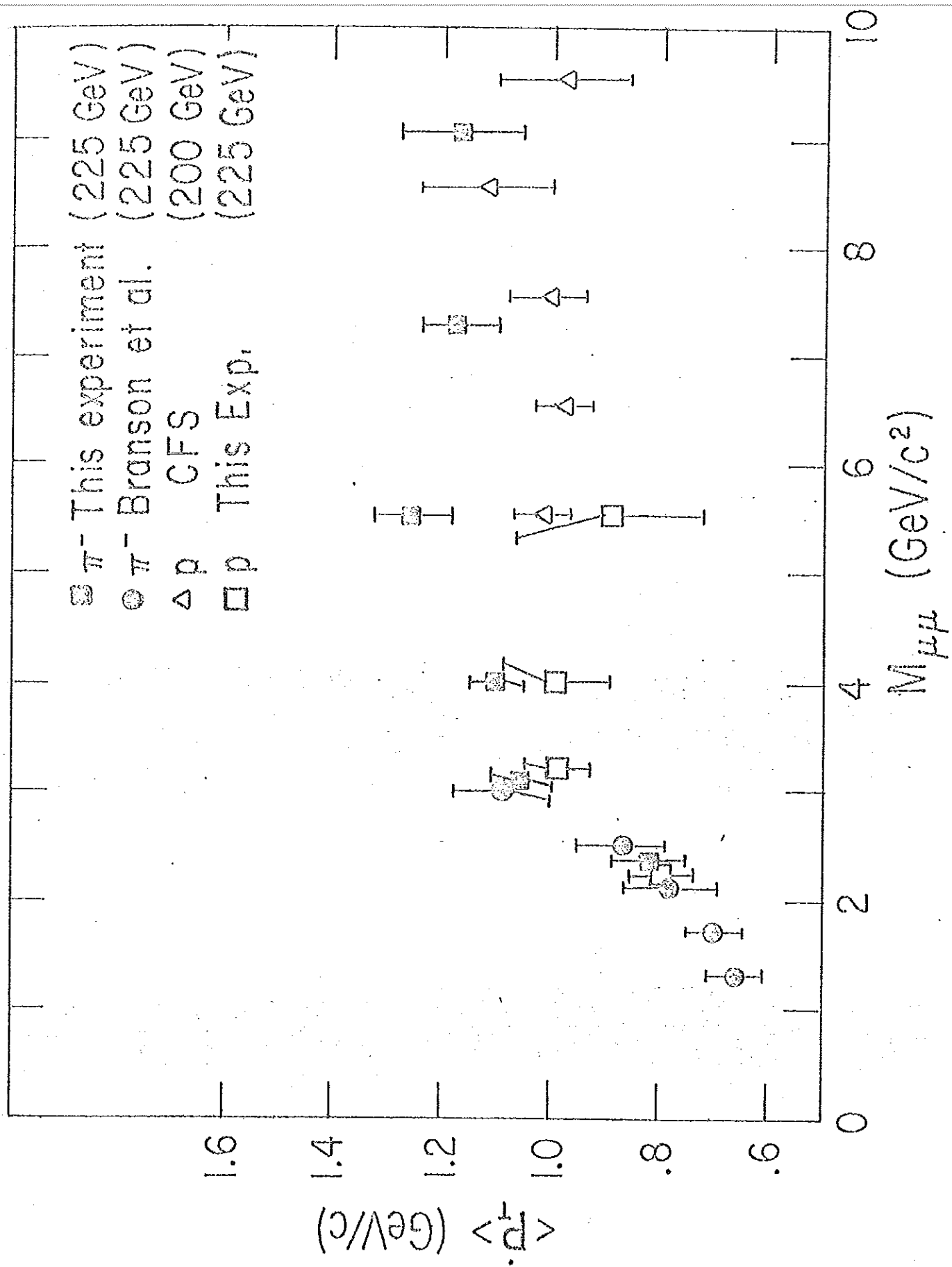


Fig. 8



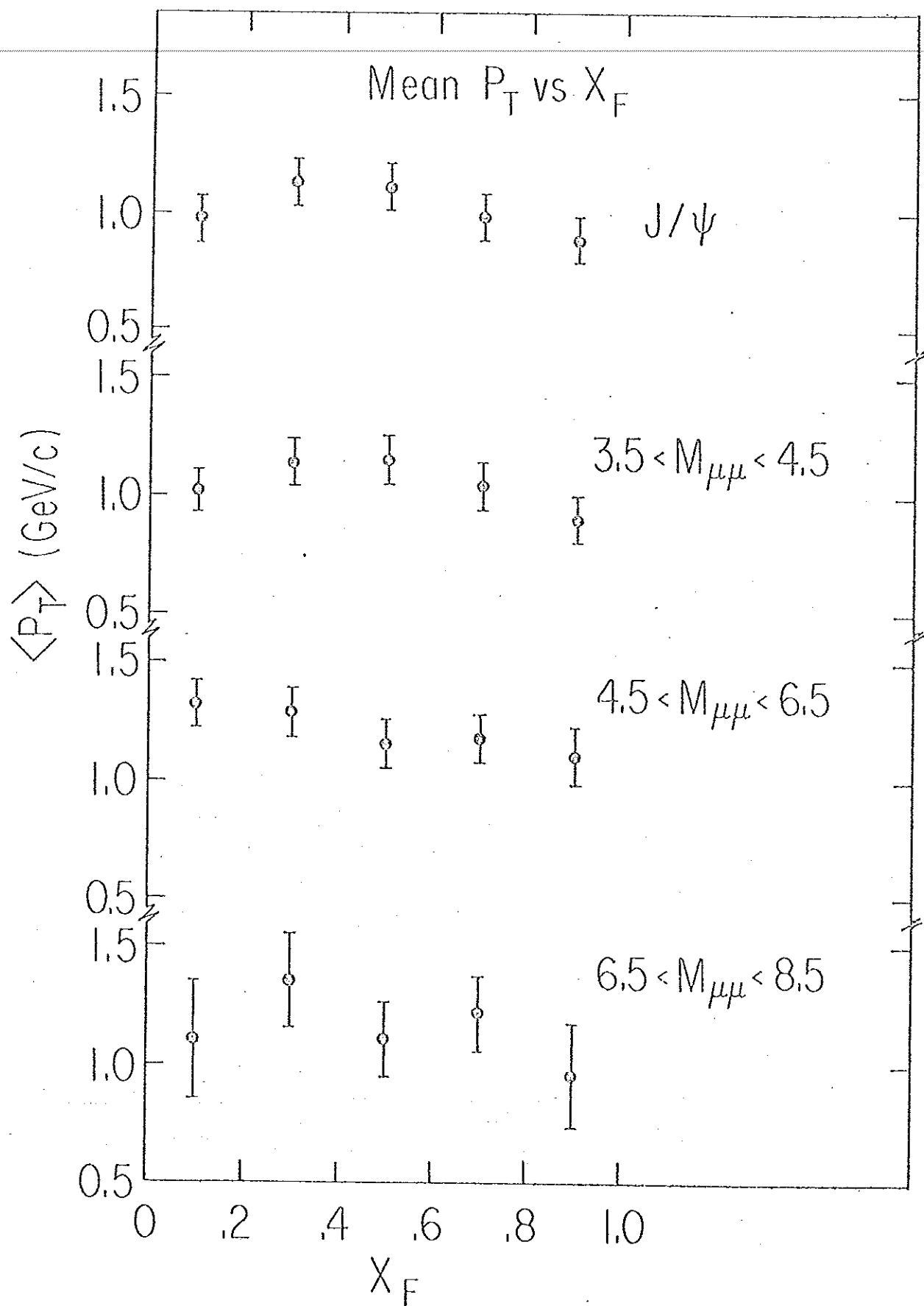


Fig. 9

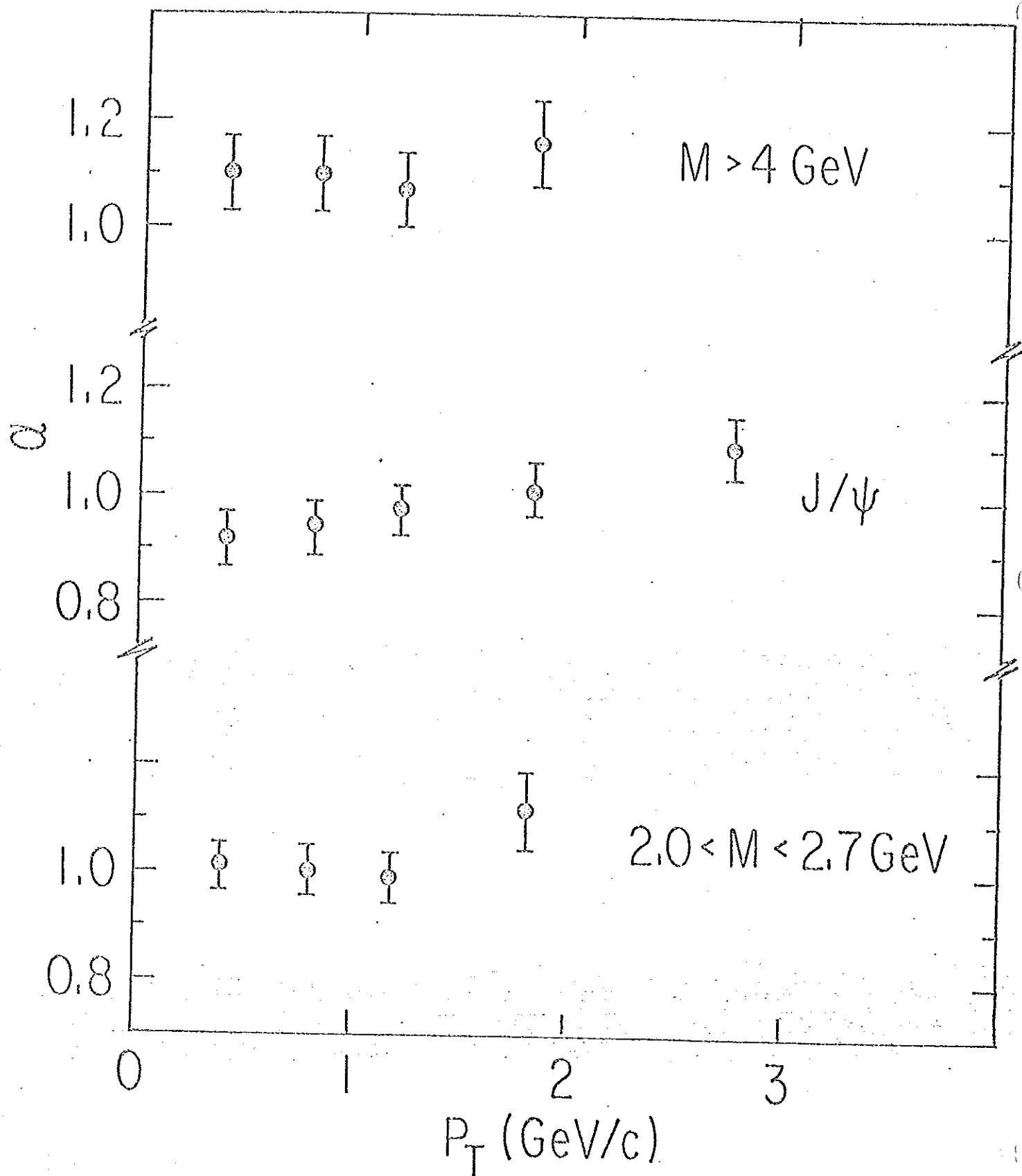


Fig. 10

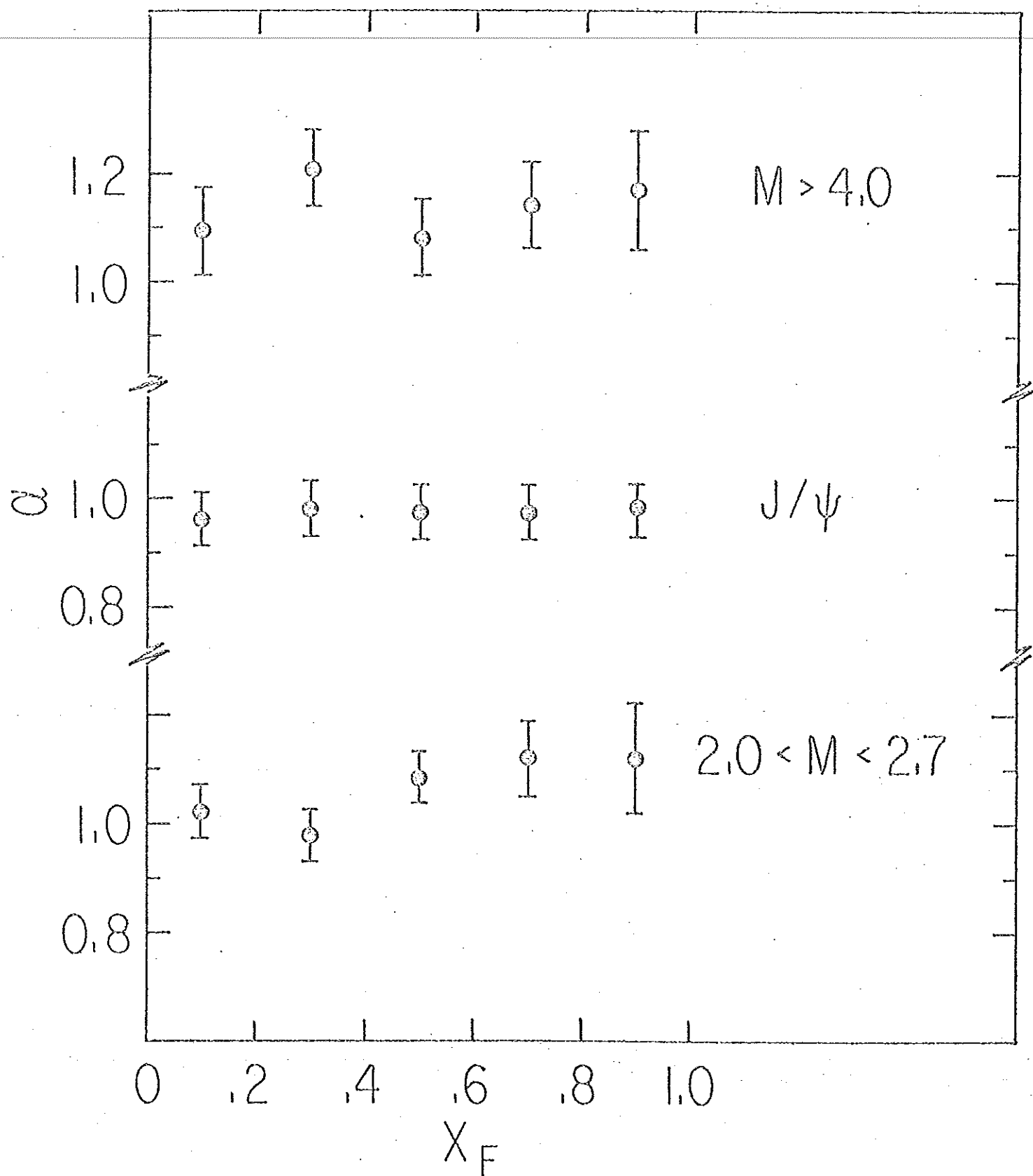


Fig. 11

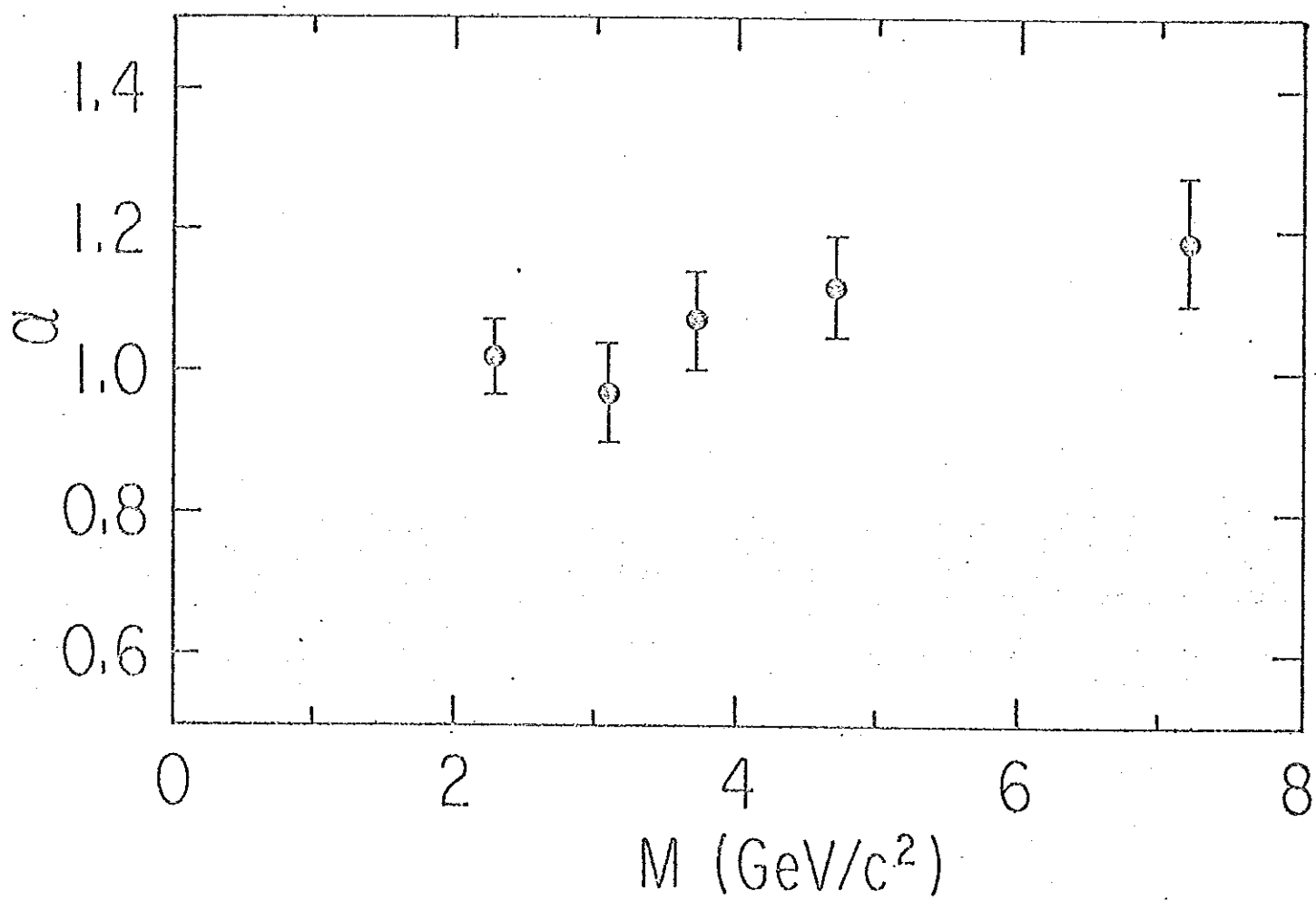


Fig. 12

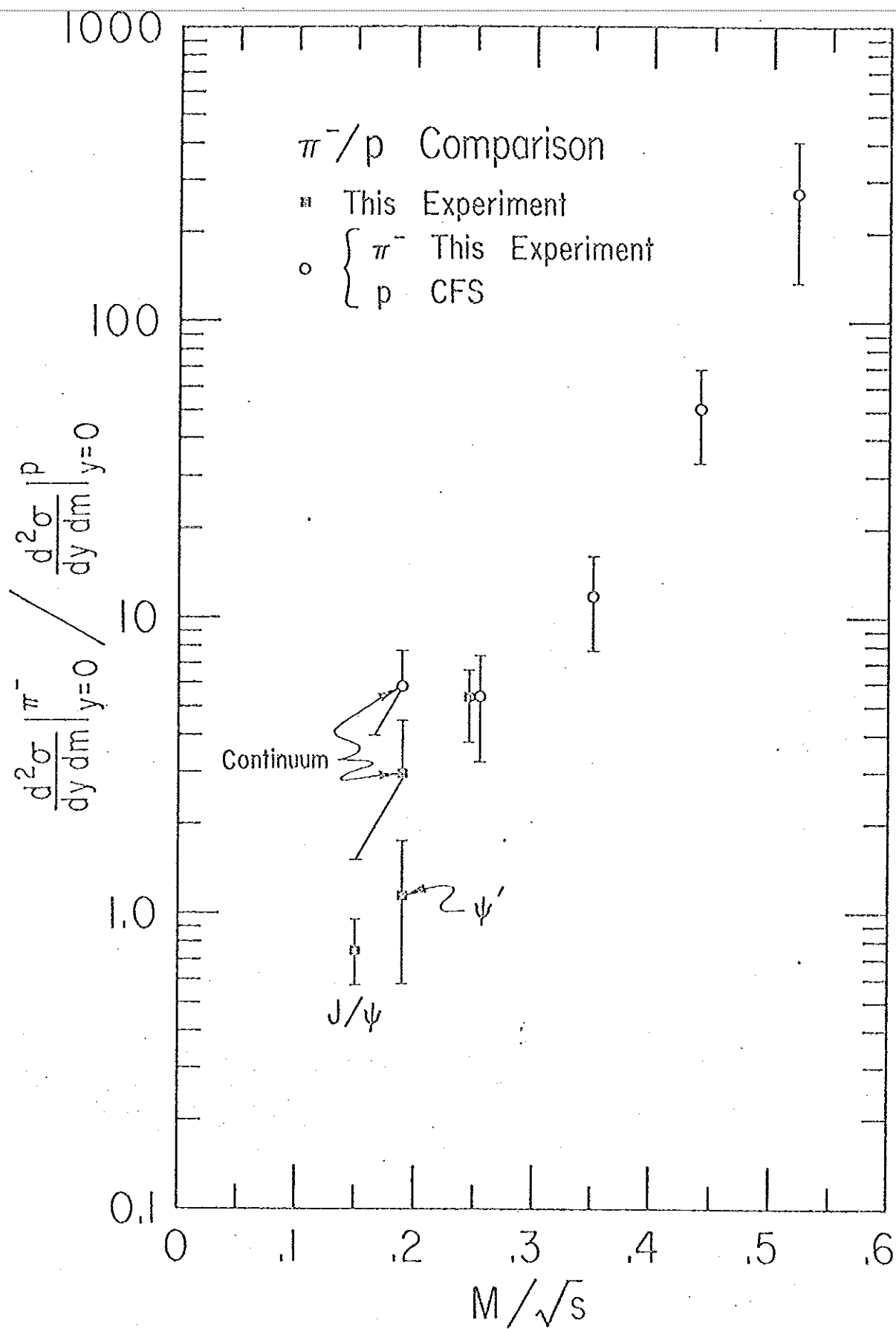
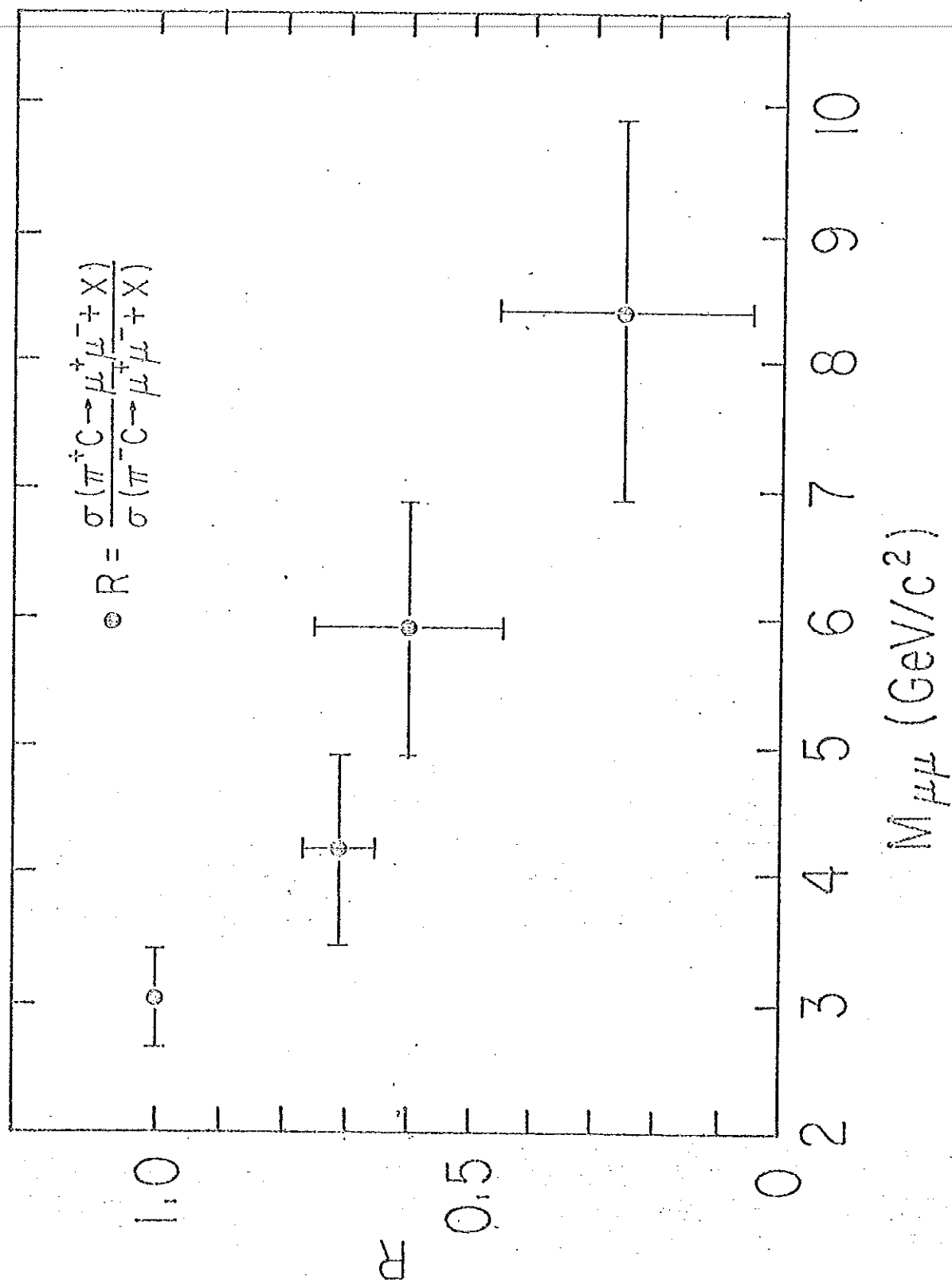
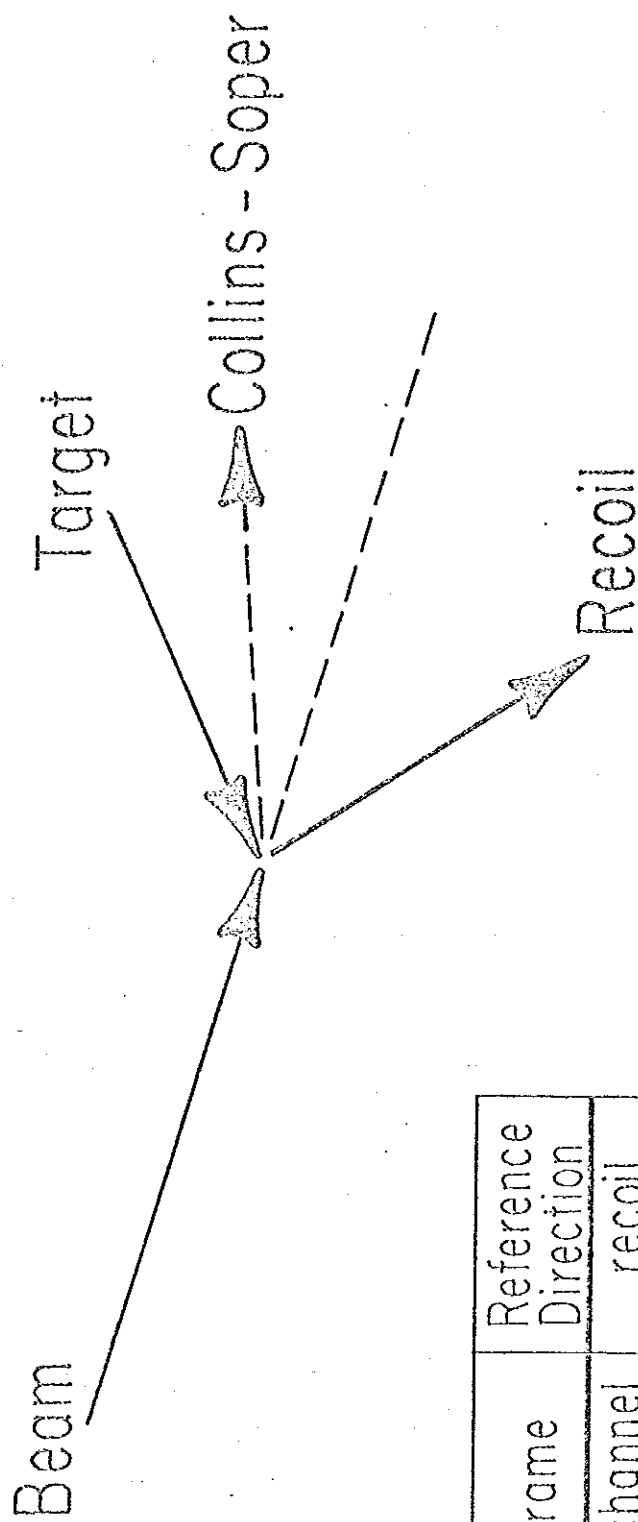


Fig. 13

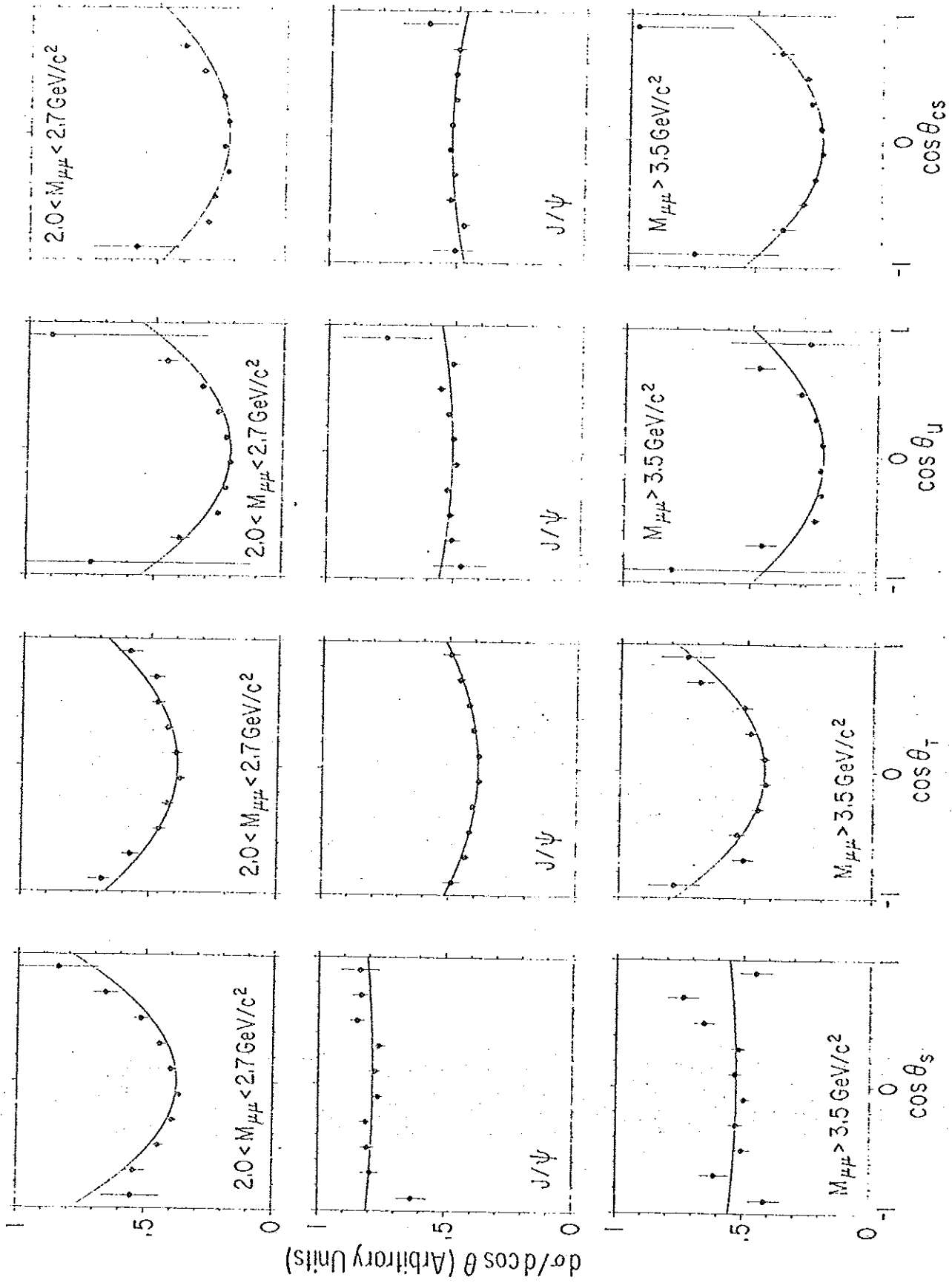




Frame	Reference Direction
s-channel	recoil
t-channel	beam
u-channel	target
Collins-Soper	$\hat{p}_B - \hat{p}_T$

# Mu - Pair C.M. System

Fig. 15





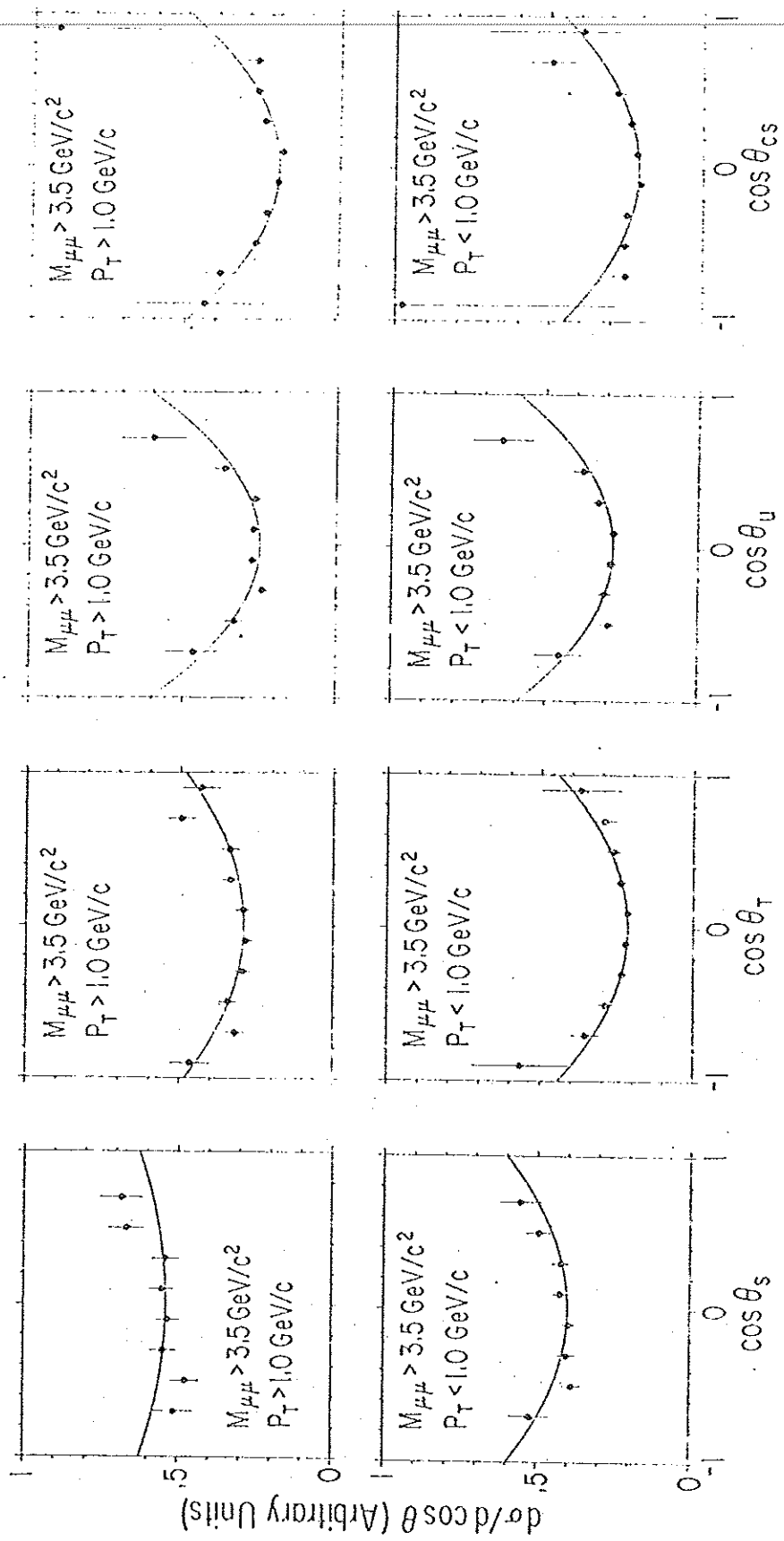


Fig. 17

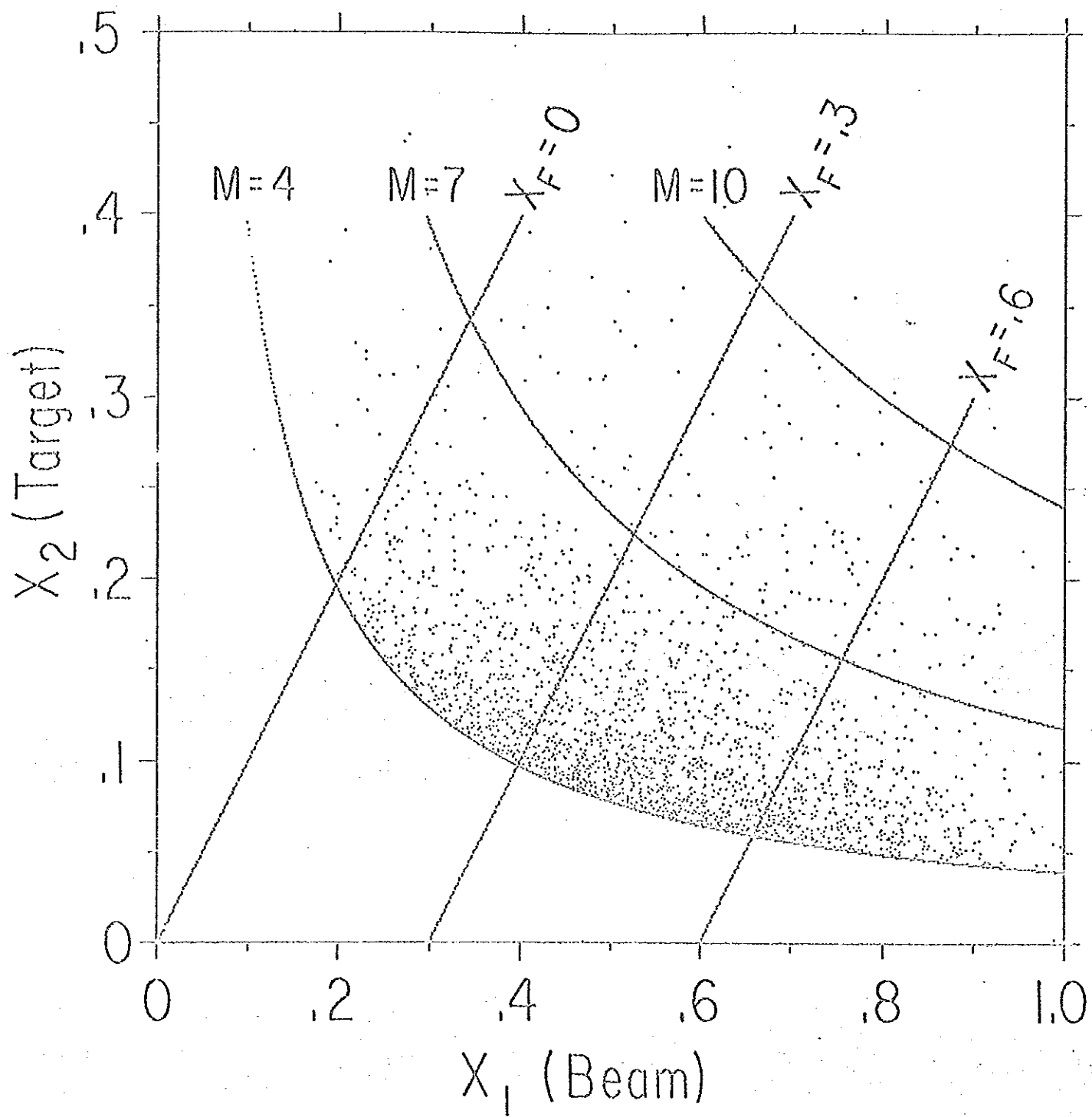


Fig. 18

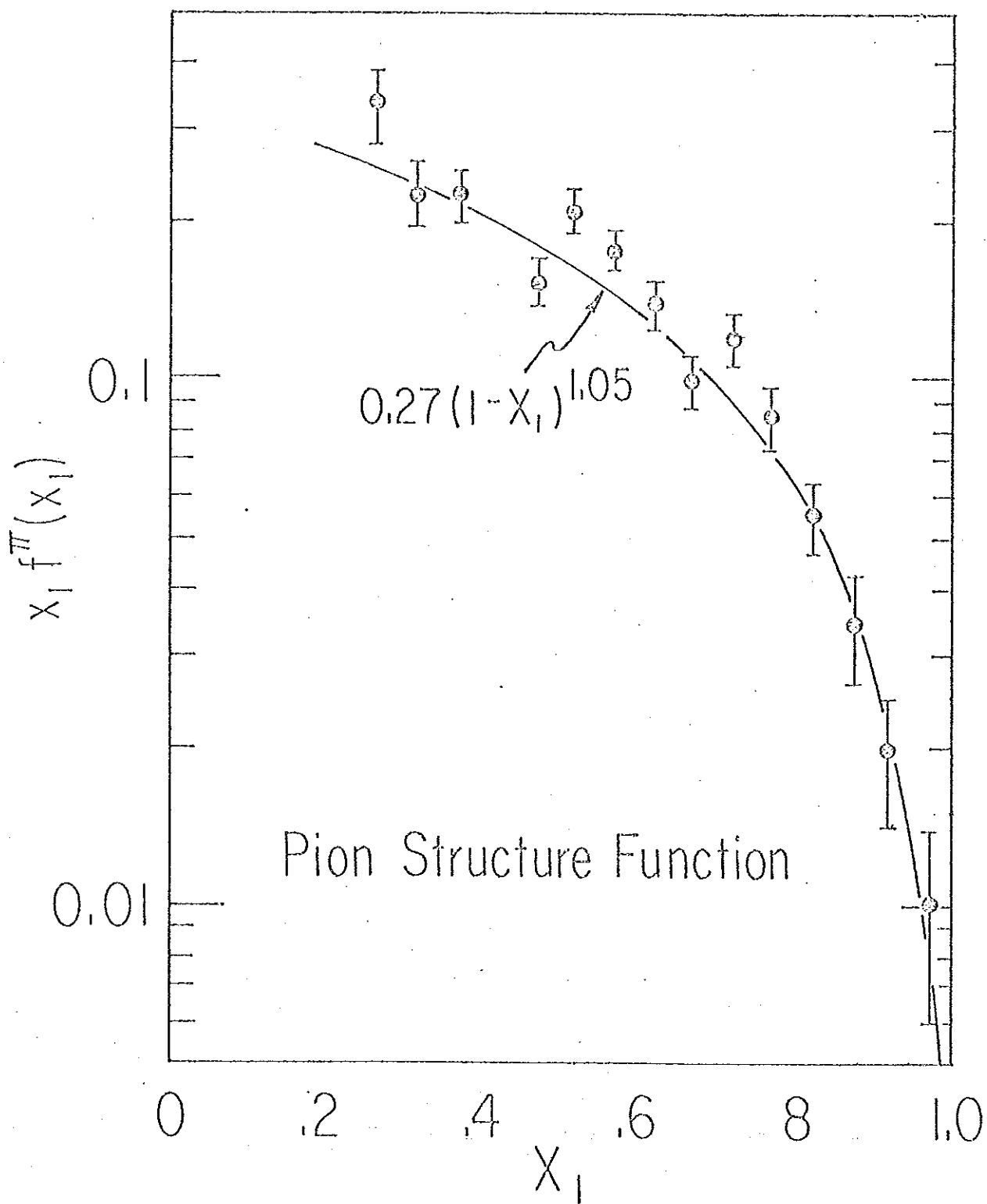


Fig. 19

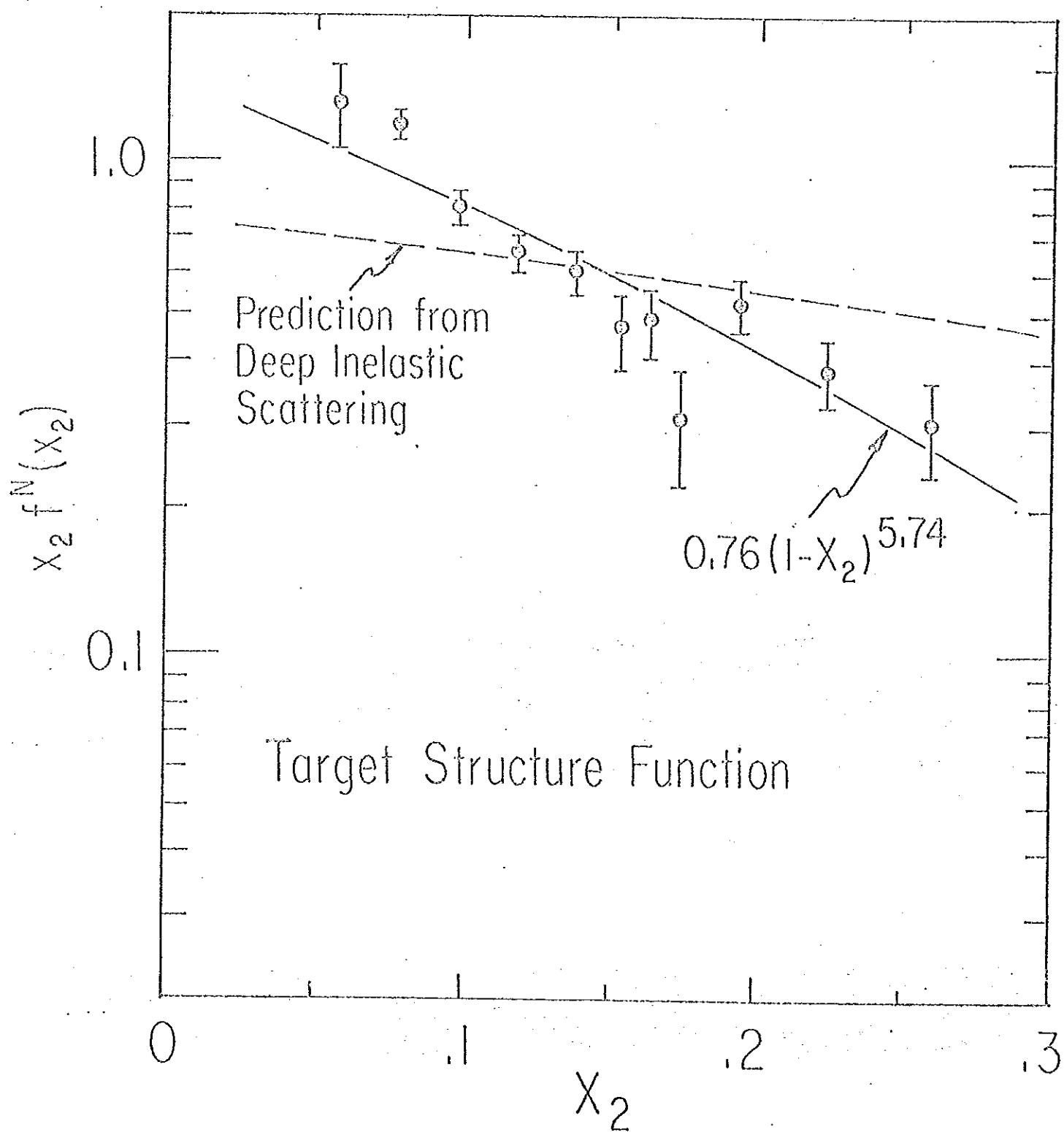


Fig. 20